Set-up of a laser system for precision spectroscopy of highly excited caesium atoms

Diplomarbeit von
Alban Urvoy
02.11.2011

Abstract

In this thesis we will present the set-up of a laser system to drive a two-photon transition to Rydberg states. The excitation is performed on a thermal atomic vapour. We observed unexpected absorption effects on the two-photon transition that were systematically explored, and that could be accounted for by a new model.

Declaration

I hereby declare that this submission is my own work and that, to the best of my knowledge and belief, it contains no material previously published or written by another person, except where due acknowledgment has been made in the text.

Alban Urvoy
Stuttgart, November 2nd, 2011

Contents

Chapter 1

Introduction

The fast development of information technology since the 1960's is characterised by Moore's law. This empirical law, first introduced by Gordon E. Moore, co-founder of Intel, in 1965, states that the number of transistor on an integrated circuit doubles approximately every two years. This evolution will however face a fundamental limit given by the size of the atoms. Therefore it is not irrelevant to watch out for new technologies suitable for computing tasks.

With the rapid development in isolating and manipulating elementary quantum systems it is now possible to implement Feynman's idea of a fundamental quantum simulator. More generally speaking is the goal of quantum information to take advantage of quantum properties such as entanglement to store and carry information on a superposition of states (a qubit) instead of 2 bits. This resource of information could then be used in a quantum computer or for quantum cryptography, which would be much more powerful and secure than any classical realisation of computers and cryptography protocols.

The quantum information theory has been heavily studied during the last decade, but to build quantum devices is still a challenge. Elementary quantum operations (CNOT-gate, single-photon source, etc.) have already been realized with systems such as trapped ions, nuclear spins or quantum dots. Also Rydberg atoms have been proposed [1] as a possible ingredient towards the realization of quantum gates, essential devices for quantum information processing. Recently this was demonstrated by two groups with two atoms. Rydberg atoms are atoms with one or several highly excited electrons. With their huge electric dipole moment, they exhibit suitable properties such as an excitation blockade which prevents more than one atom to be excited in a Rydberg state within a certain blockade radius.

Based on this Rydberg atoms in vapour cells are a promising system for the realization of quantum devices as for their scalability. It has been shown that Rydberg excitation is possible in confinement [2], and more recently, that fast coherent Rabi oscillations with a Rydberg state can occur [3]. Caesium appears to be a better candidate to explore quantum information technology due to higher vapour pressure, larger hyperfine structure and better suited laser systems.

This thesis presents a new coherent excitation scheme to Rydberg states for this purpose.

Chapter 2

Fundamental aspects

This chapter presents fundamental aspects that are needed to understand the results present in this this thesis. In the first section the properties of the element caesium are detailed. The theoretical foundations of atom-light interaction are discussed in the second section. An brief introduction to the dipole matrix element formalism is given in the third section. The discrepancies of real systems to the theoretical treatment are discussed in the fourth section.

2.1 The element caesium

Caesium is is the second heaviest alkali element, and the heaviest to have a stable isotope. Only ^{133}Cs is stable, and we will consider only this isotope in the following study. Useful physical properties of ^{133}Cs are listed in Table 2.1. The vapour pressure formulae for caesium are given in [4]. For the temperature range relevant for this thesis (room temperature up to $200\,^\circ$C), caesium has a vapour pressure that is low enough for the ideal gas model to apply. From the ideal gas law and the vapour pressure formula one can obtain the expression for the atomic density of caesium in the gas phase as a function of the temperature (in Kelvin):

$$n(T) = \frac{1.0133 \cdot 10^{9.165 - \frac{3830}{T}}}{k_B T} \tag{2.1}$$

2.2 Atom-light interaction

The theoretical treatment of atom-light interaction in two and three-level systems has been performed in a variety of books and theses. In the following we will present the models and the necessary formulae for this thesis. The derivation of these formulae can be found in [5], [6].

Atomic number	Z	55
Atomic mass number	A	133
Atomic mass	m	$2.206\,946\,57(11) \times 10^{-25}\,\text{kg}$
Nuclear spin	I	7/2
Melting point	T_M	$28.5\,^\circ$C
Vapour pressure at $25\,^\circ$C	P_V	$1.983(98) \times 10^{-6}\,\text{mbar}$

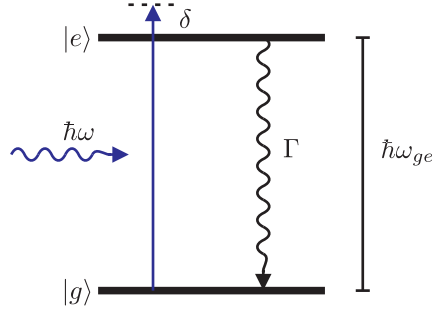Table 2.1: Useful physical properties of ^{133}Cs [4].

Figure 2.1: Two-level system coupled to a light field. ω is the light frequency, ω_{ge} the absolute frequency of the transition, δ the detuning of the light field with respect to the transition frequency and γ the decay rate from the excited state $|e\rangle$ to the ground state $|g\rangle$.

2.2.1 Two-level atom

The simplest way to describe the interaction of a light with atoms is to consider a classical light field and a two-level system. We consider a ground state $|g\rangle = \binom{1}{0}$ and an excited state $|e\rangle = \binom{0}{1}$. The system is shown in Figure 2.1. The Hamilton operator for the purely atomic system is the following:

$$H_A = \hbar \begin{pmatrix} 0 & 0 \\ 0 & \omega_{ge} \end{pmatrix} \tag{2.2}$$

The Hamiltonian describing the interaction between this two-level atom and a classical light field $E(t) = E_0(e^{i\omega t} + e^{-i\omega t})$ is:

$$H_{AL} = -d_{ge}E(t) \begin{pmatrix} 0 & 1 \\ 1 & 0 \end{pmatrix} \tag{2.3}$$

where d_{ge} is the dipole matrix element of the transition.
By introducing the Rabi frequency $\Omega_{ge} = \frac{-d_{ge}E_0}{\hbar}$ and applying the rotating wave approximation, the Hamiltonian reduces to:

$$H = \hbar \begin{pmatrix} 0 & \Omega_{ge}/2 \\ \Omega_{ge}/2 & -\delta \end{pmatrix} \tag{2.4}$$

The system can be described by the density matrix

$$\rho = \begin{pmatrix} \rho_{gg} & \rho_{ge} \\ \rho_{eg} & \rho_{ee} \end{pmatrix} \tag{2.5}$$

and the decay process from the excited state is accounted for by the Lindblad operator

$$L(\rho) = \Gamma \begin{pmatrix} \rho_{ee} & -\frac{1}{2}\rho_{ge} \\ -\frac{1}{2}\rho_{eg} & -\rho_{ee} \end{pmatrix}. \tag{2.6}$$

The time evolution of the system is described by the Liouville-von Neumann equation:

$$\frac{\partial \rho}{\partial t} = -\frac{i}{\hbar}[H, \rho] + L(\rho) \tag{2.7}$$

8

The equations verified by each coefficient of the density matrix are:

$$\dot{\rho}_{gg} = \frac{i\Omega_{ge}}{2}(\rho_{ge} - \rho_{eg}) + \Gamma\rho_{ee}$$

$$\dot{\rho}_{ge} = \frac{i\Omega_{ge}}{2}(\rho_{gg} - \rho_{ee}) - \left(\frac{\Gamma}{2} + i\delta\right)\rho_{ge}$$

$$\dot{\rho}_{eg} = \frac{i\Omega_{ge}}{2}(\rho_{ee} - \rho_{gg}) - \left(\frac{\Gamma}{2} - i\delta\right)\rho_{eg}$$

$$\dot{\rho}_{gg} = \frac{i\Omega_{ge}}{2}(\rho_{eg} - \rho_{ge}) - \Gamma\rho_{ee}$$

(2.8)

With the hypothesis that $\rho_{gg} + \rho_{ee} = 1$, the steady state solutions are:

$$\rho_{gg} = \frac{\Omega_{ge}^2 + 4\delta^2 + \Gamma^2}{2\Omega_{ge}^2 + 4\delta^2 + \Gamma^2}$$

$$\rho_{ge} = \frac{\Omega_{ge}(i\Gamma + 2\delta)}{2\Omega_{ge}^2 + 4\delta^2 + \Gamma^2}$$

$$\rho_{eg} = \frac{\Omega_{ge}(i\Gamma - 2\delta)}{2\Omega_{ge}^2 + 4\delta^2 + \Gamma^2}$$

$$\rho_{gg} = \frac{\Omega_{ge}^2}{2\Omega_{ge}^2 + 4\delta^2 + \Gamma^2}$$

(2.9)

We can define the saturation parameter as

$$\frac{I}{I_{sat}} = 2\left(\frac{\Omega_{ge}}{\Gamma}\right)^2$$

(2.10)

so that the previous coherences in steady-state transform to

$$\rho_{gg} = \frac{1 + \frac{1}{2}\frac{I}{I_{sat}} + 4\left(\frac{\delta}{\Gamma}\right)^2}{1 + \frac{I}{I_{sat}} + 4\left(\frac{\delta}{\Gamma}\right)^2}$$

$$\rho_{ee} = \frac{\frac{1}{2}\frac{I}{I_{sat}}}{1 + \frac{I}{I_{sat}} + 4\left(\frac{\delta}{\Gamma}\right)^2}$$

$$\rho_{ge} = \frac{\frac{1}{\sqrt{2}}\sqrt{\frac{I}{I_{sat}}}\left(i + 2\frac{\delta}{\Gamma}\right)}{1 + \frac{I}{I_{sat}} + 4\left(\frac{\delta}{\Gamma}\right)^2} = \rho_{eg}^*$$

(2.11)

where $I = \frac{c\epsilon_0 E_0^2}{2}$ is the light intensity. The saturation intensity is given by:

$$I_{sat} = \frac{c\epsilon_0\Gamma^2\hbar^2}{4d_{ge}^2}$$

(2.12)

Light absorption

The polarisation of the atom is given by the expectation value of the dipole moment $\langle d \rangle$ and the atomic density:

$$P = n \cdot \langle d \rangle = n \cdot (d_{ge}^*\rho_{ge} + d_{ge}\rho_{eg}^*)$$

(2.13)

Moreover the response of the polarisation of the atoms to weak electric fields is linear:

$$P = \epsilon_0\chi E$$

(2.14)

9

The imaginary part of the susceptibility χ contains the information about the absorption properties. We can therefore extract the absorption coefficient $\alpha_0 = \frac{\omega}{c} \operatorname{Im} \chi$. Note that the absorption coefficient is proportional to the imaginary part of the coherence between the two states. We obtain the absorption coefficient:

$$
\begin{aligned}
\alpha_0 &= \frac{\omega}{c} \frac{n}{\epsilon_0 E_0} \cdot 2 d_{ge} \operatorname{Im} \rho_{ge} \\
&= n \, \sigma_0 \frac{1}{1 + \frac{I}{I_{sat}} + 4(\frac{\delta}{\Gamma})^2} \\
&= n \, \sigma(\delta, I)
\end{aligned}
\tag{2.15}
$$

with $\sigma(\delta, I) = \sigma_0 \frac{1}{1 + \frac{I}{I_{sat}} + 4(\frac{\delta}{\Gamma})^2}$ and $\sigma_0 = \frac{\hbar \omega \Gamma}{2 I_{sat}}$ being the absorption cross section and the resonant absorption cross section.

Absorption of a Doppler-broadened medium

The atomic ensembles that we are considering in this thesis are atomic vapours at room temperature or even above so that the thermal movement of the atoms cannot be neglected. Each atom, moving with its velocity $\vec{v}$, experiences the Doppler effect in its interaction with the light field. If ω is the light frequency in the laboratory frame of reference, the light frequency in the frame of reference of the atom is $\omega' = \omega - \vec{k} \cdot \vec{v}$. The atomic velocity follows a Maxwell-Boltzmann distribution, so it can be shown that the number of atoms that resonant with the light field as a function of detuning δ to the absolute frequency of the transition is given by:

$$
n(\delta) d\delta = n_0 \sqrt{\frac{mc^2}{2\pi k_B T \omega}} e^{-\frac{mc^2 \delta^2}{2 k_B T}} d\delta
\tag{2.16}
$$

where n_0 is the atomic density, c the speed of light, k_B the Boltzmann constant, T the temperature and m the atomic mass.

The absorption coefficient is then defined by equation (2.15) any more but by the convolution of $n(\delta)$ and $\sigma(\delta, I)$.

In the low intensity regime, one can neglect the power broadening effect. Moreover, the linewidth of the excited state (typically a few MHz) is small compared to the width of the Doppler broadened absorption profile (typically a few hundreds of MHz at room temperature). The absorption coefficient can then be approximated to have a Gaussian lineshape. The width of this Gaussian profile $n(\delta)$, the so-called Doppler width (FWHM) is given by (from [7]):

$$
\omega_D = \frac{\omega}{c} \sqrt{\frac{8 \ln 2 k_B T}{m}}
\tag{2.17}
$$

The formula of the absorption coefficient for a single atomic transition is therefore (from [7]):

$$
\alpha = n_0 \sigma_0 \frac{\pi \Gamma}{2} \sqrt{\frac{\ln 2}{\pi}} \frac{2}{\omega_D} e^{-4 \ln 2 (\frac{\delta}{\omega_D})^2}
\tag{2.18}
$$

2.2.2 Three-level atom

In this thesis, we report on Rydberg excitation of caesium atoms via an intermediate state. A similar theoretical approach to the one presented in section 2.2.1 can be use to describe such a three-level system. We add to the previous system from Figure 2.2.1 a third level of higher energy that is coupled to a second light field. The two light fields can be written as $E_i(t) = E_{i,0}(e^{i\omega_i t} + e^{-i\omega_1 t})$ with $i = 1, 2$ for the first and second transition. This so-called
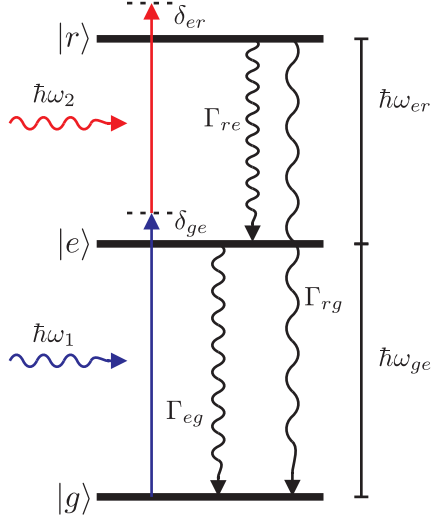
Figure 2.2: Three-level ladder-type system coupled to two light fields. $|g\rangle$, $|e\rangle$ and $|r\rangle$ are the ground state, intermediate state and upper/Rydberg state. ω_1 (resp. ω_2) is the frequency of the light field coupling the first (resp. second) transition, ω_{ge} (resp. ω_{er}) the absolute frequency of the first (resp. second) transition, δ_{ge} (resp. δ_{er}) the detuning of the first (resp. second) light field with respect to the first transition frequency, and Γ_{ji} the decay rate from the $|j\rangle$ state to the $|i\rangle$ state.

three-level ladder-type system is shown in Figure 2.2. We can represent the three states in the following way:

$$|g\rangle = \begin{pmatrix} 1 \\ 0 \\ 0 \end{pmatrix} \quad |e\rangle = \begin{pmatrix} 0 \\ 1 \\ 0 \end{pmatrix} \quad |r\rangle = \begin{pmatrix} 0 \\ 0 \\ 1 \end{pmatrix}$$

and the density matrix for the system is therefore

$$\rho = \begin{pmatrix} \rho_{gg} & \rho_{ge} & \rho_{gr} \\ \rho_{eg} & \rho_{ee} & \rho_{er} \\ \rho_{rg} & \rho_{re} & \rho_{rr} \end{pmatrix}.$$

Similarly to the two-level atom, d_{ge} (resp. d_{er}) is the dipole matrix element of the first (resp. second) transition, and we can define the Rabi-frequencies describing the coupling of the light field to the transition by $\Omega_{ge} = \frac{-d_{ge}E_{0,1}}{\hbar}$ and $\Omega_{er} = \frac{-d_{er}E_{0,2}}{\hbar}$. After applying the rotating wave approximation, the Hamiltonian describing the atom and the atom-light interaction is

$$H = \begin{pmatrix} 0 & \Omega_{eg}/2 & 0 \\ \Omega_{eg}/2 & -\delta_{ge} & \Omega_{er}/2 \\ 0 & \Omega_{er}/2 & -\delta_{er} - \delta_{ge} \end{pmatrix}. \tag{2.19}$$

Once again, the Liouville-von Neumann equation describes the time evolution of the system:

$$\frac{\partial \rho}{\partial t} = -\frac{i}{\hbar}[H, \rho] + L(\rho) \tag{2.20}$$

where the dissipative effects are accounted for by the new Lindblad operator

$$L(\rho) = \begin{pmatrix} \Gamma_{eg}\rho_{ee} + \Gamma_{rg}\rho_{rr} & -\frac{1}{2}\Gamma_{eg}\rho_{ge} & -\frac{1}{2}\left(\Gamma_{re} + \Gamma_{rg}\right)\rho_{gr} \\ -\frac{1}{2}\Gamma_{eg}\rho_{eg} & -\Gamma_{eg}\rho_{ee} + \Gamma_{re}\rho_{rr} & -\frac{1}{2}\left(\Gamma_{re} + \Gamma_{rg} + \Gamma_{eg}\right)\rho_{er} \\ -\frac{1}{2}\left(\Gamma_{re} + \Gamma_{rg}\right)\rho_{rg} & -\frac{1}{2}\left(\Gamma_{re} + \Gamma_{rg} + \Gamma_{eg}\right)\rho_{re} & -\left(\Gamma_{re} + \Gamma_{rg}\right)\rho_{rr} \end{pmatrix}. \tag{2.21}$$

11

Note that the coherence between two states decay with the sum of the half decay rates of these states.

Similarly to the two-level atom, the absorption of a light field is here as well proportional to the imaginary part of the coherence corresponding to the driven transition.

Electromagnetically induced transparency

In a three-level system, some peculiar effects can arise, such as electromagnetically induced transparency (EIT). EIT has been studied and discussed since its first observation in 1991 [8], as it carries promising properties for the realisation of non-classical optical devices. The basic principle of EIT can be understood with a simple picture.

In a three-level ladder-type system, EIT is observed with weak probe field on the first transition ($|1\rangle \to |2\rangle$) as a strong pump field drives the second transition. The strong pump field modifies the properties of of the atomic medium for the probe field, and the absorption on the first transition is eliminated on resonance. This phenomena can be explained in terms of quantum interference between the excitation pathways to the intermediate state ($|1\rangle \to |2\rangle$ and $|1\rangle \to |2\rangle \to |3\rangle \to |1\rangle$). On resonance these interfere destructively so that the absorption is annihilated. More comprehensive studies on EIT can be found in [1].

2.3   Dipole matrix element formalism

In real atomic systems, the atomic levels are degenerated in magnetic sublevels. Depending on the magnetic quantum number m of the magnetic sublevel and the polarisation of the light field, the dipole matrix elements take different values. If we consider two hyperfine sublevels $|Fm_F\rangle$ and $|F'm'_F\rangle$, the dipole matrix element that couples them is $\langle Fm_F|er_q|F'm'_F\rangle$, where q describes the angular component of the position operator $\boldsymbol{r}$ (see section B.1.1). The angular dependence can be factorized using the Wigner-Eckart theorem into:

$$\langle Fm_F|er_q|F'm'_F\rangle = \langle F\|e\boldsymbol{r}\|F'\rangle(-1)^{F'-1+m_F}\sqrt{2F+1}\begin{pmatrix} F' & 1 & F \\ m'_F & q & -m_F \end{pmatrix} \tag{2.22}$$

where $\langle F\|e\boldsymbol{r}\|F'\rangle$ is the so-called reduced dipole matrix element and the (:::) symbol is the Wigner 3-j symbol. This reduced dipole matrix element can be further factorised into terms that do not depend on the hyperfine coupling between the total angular momentum J and the nuclear spin I, and on the spin-orbit coupling between the azimuthal angular momentum and the electronic spin:

$$\langle F\|e\boldsymbol{r}\|F'\rangle = \langle J\|e\boldsymbol{r}\|J'\rangle(-1)^{F'+J+1+I}\sqrt{(2F'+1)(2J+1)}\begin{Bmatrix} J & J' & 1 \\ F' & F & I \end{Bmatrix} \tag{2.23}$$

$$\langle J\|e\boldsymbol{r}\|J'\rangle = \langle L\|e\boldsymbol{r}\|L'\rangle(-1)^{J'+L+1+S}\sqrt{(2J'+1)(2L+1)}\begin{Bmatrix} L & L' & 1 \\ J' & J & S \end{Bmatrix} \tag{2.24}$$

where the {:::} symbol is the Wigner 6-j symbol.

These formulae yield the relative strength of every single transition between two hyperfine sublevels from a $L \to L'$ transition.

The derivation of the previous formulae is detailed in section B, as well as some discussions about the dipole matrix elements.

2.4   Real systems

The theoretical treatment of the atom-light interaction presented in section 2.2 describes the basics of these interactions. However, except for the case of a cyclic transition (perfect two-level
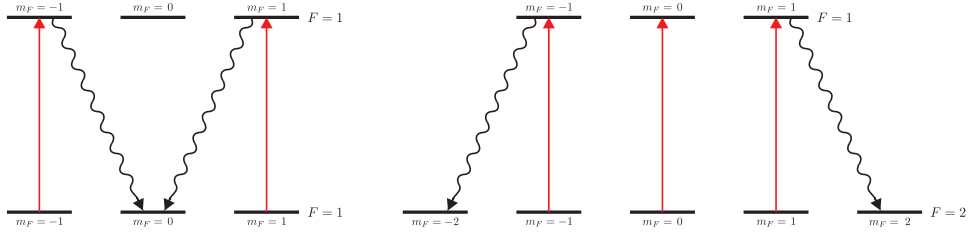
Figure 2.3: Optical pumping in transitions with $F' = F - 1$ and $F' = F$. The allowed transitions for linearly polarised light fields and the decays into the dark state are shown.

system), this two-level model gets strongly perturbed by several effects when it comes to describe the interaction of a light field with an atomic ensemble. In this section we will first describe the processes that perturb an atomic system from the two-level system, and notice that some of these cancel each other. In the whole section we will only consider linearly polarised light fields.

2.4.1 Deviations from the two-level model

Manifold optical pumping

Let us first consider a real $F \to F'$ atomic transition. As mentioned above each transition between two hyperfine states has a specific dipole matrix element. Moreover, each excited hyperfine state has specific decay rates on the allowed transition. Therefore the steady state distribution of the atoms on a magnetic manifold is not an equal distribution. Typically the atoms are being pumped around the central hyperfine state $m_F = 0$.

The derivation of this optical pumping for the case of $F' = F + 1$ was performed by Gao [9]. The interesting consequence of his results is that the coupling to the excited state is affected and that the two-level model remains valid with the effective dipole moment verifying

$$d_{eff}^2 = g_S(2F + 1)|\langle F \| e\boldsymbol{r} \| F' \rangle|^2. \tag{2.25}$$

For a transition $F = 4 \to F' = 5$ (caesium D2-line $6S_{\frac{1}{2}} \to 6P_{\frac{3}{2}}$), $g_S = \frac{4420}{92377} = 0.047\,847\,4$. For the two other allowed cases $F' = F - 1$ and $F' = F$ one or two of the magnetic sublevels are dark states (see Figure 2.3). Hence the atoms are pumped into these dark states and in the steady-state there is no absorption anymore.

Optical pumping in the dark ground state

Another optical pumping effect can occur in the interaction of a light field with an ensemble of atoms. At least with alkali atoms, because of the hyperfine coupling between the total angular momentum and the nuclear spin, the ground state is split. So, when the light field is resonant to one atomic transition, the other ground state is a *dark state*. If the transition between the excited state and the dark ground state is dipole-allowed, then the atoms are pumped into the dark ground state and there is once again no steady-state absorption.

According to this, the absorption of the D1-line of caesium ($6S_{\frac{1}{2}}(F = 3, 4) \to 6P_{\frac{1}{2}}(F' = 3, 4)$) in the steady state should always be zero. This cannot be true since, as we will see in section 3.3, a laser resonant to the D1-line of caesium is absorbed.

Transit time broadening

As mentioned above the atoms are moving. Moreover, the interaction is performed by a laser of finite beam cross section. So the atoms only spend a limited time interacting with the light

field.

This effect is called the transit time broadening. The interaction time between the light field and the atom is given by the ratio of the atomic velocity to the path length through beam. After this interaction time τ, the atom leaves the beam section and is basically replaced by a new atom at a random ground state sublevel. If we assume the light intensity to be weak enough, we can consider the excited state population to be negligible so that no excited atom leaves the beam section. The transit time broadening can therefore be regarded as a decay to every ground state with the same decay rate $\Gamma_{tt} = 1/\tau$. The tricky part is to determine a value for this decay rate. The difficulty is originating from two facts: the atomic velocity is Maxwell-Boltzmann-distributed and the laser beam profile is Gaussian. Sagle et al. [10] conducted a theoretical and experimental investigation on transit time effects on the D1-line of caesium. For the atomic velocity, they worked with the two-dimensional mean velocity $\overline{v} = \sqrt{\frac{\pi k_B T}{2m}}$. Then they matched their theoretical and experimental results and determined that the appropriate beam diameter to use for the mean path length through the beam is the full width at half maximum (FWHM). The average path length is $\overline{d} = \frac{\pi D_{1/2}}{4}$, $D_{1/2}$ being the FWHM beam diameter. So according to Sagle et al., a good expression for the transit time decay rate is:

$$\Gamma_{tt} = \overline{v}/\overline{d} = \frac{1}{D_{1/2}}\sqrt{\frac{8k_B T}{\pi m}} = \frac{1}{\sqrt{\log 2}D_{1/e^2}}\sqrt{\frac{8k_B T}{\pi m}} \tag{2.26}$$

with D_{1/e^2} being the beam full width at $\frac{1}{e^2}$ maximum. From this expression, a typical value for transit time decay rate with caesium atoms is $\Gamma_{tt} = 2\pi \times 36\,\text{kHz}$ (at $60\,^{\circ}\text{C}$ with $D_{1/2} = 1\,\text{mm}$). So the finite transit time of the atoms in the light field prevents the atomic ensemble to reach the expected steady state that would show no absorption, in the case where the atoms would be pumped to dark states of the magnetic manifold or to the dark ground state. In the case where there is no dark state for the system, the transit time broadening tends to flatten the distribution of the atoms over the magnetic manifold.

Chapter 3

The $6S \to 7P$ transition in caesium

In this chapter the results of our measurements on the $6S_{\frac{1}{2}} \to 7P_{\frac{3}{2}}$ transition of caesium, the first transition of the three-level system described in chapter 4, are presented. This transition is driven with a commercial frequency doubled amplified diode laser (Toptica TA-SHG Pro) at 455 nm. We first have a look at the level scheme of this transition. In the second section, the laser locking set-up scheme is described, as well as its optimization. In the third section we present further measurements to determine the temperature of the spectroscopy cell.

3.1   Level scheme

The $6S_{\frac{1}{2}} \to 7P_{\frac{3}{2}}$ transition is quite similar to the well-known $6S_{\frac{1}{2}} \to 6P_{\frac{3}{2}}$ transition (D2-line) of caesium. The hyperfine structure of these two levels is shown in Figure 3.1. The reduced dipole matrix element for this transition was determined experimentally [11] to be

$$\left\langle J = \tfrac{1}{2} \middle\| e\boldsymbol{r} \middle\| J' = \tfrac{3}{2} \right\rangle_{6S_{\frac{1}{2}} \to 7P_{\frac{3}{2}}} = 0.4965(35) \times 10^{-29}\,\mathrm{C \cdot m} \tag{3.1}$$

Besides the characteristic frequencies and dipole matrix elements, the main difference of this transition to the D2-line of caesium is that this system is not a closed system. That means that $7P_{\frac{3}{2}} \rightsquigarrow 6S_{\frac{1}{2}}$ is not the only allowed decay channel from the $7P_{\frac{3}{2}}$ state (see Figure 3.2). All decay channels from the $7P_{\frac{3}{2}}$ state, along with the lifetimes and transition probabilities are shown in Figure 3.2.

The total lifetime of the $7P_{\frac{3}{2}}$ state is defined as

$$\frac{1}{\tau} = \sum_i \Gamma_i \tag{3.2}$$

where the Γ_i are the transition probabilities from the $7P_{\frac{3}{2}}$ state. The formula shown above gives a lifetime of $\tau = 111$ ns. The lifetime of the $7P_{\frac{3}{2}}$ state has been measured before as $\tau_{exp} = 134.5$ ns ($\Gamma_{exp} = 2\pi \cdot 1.18$ MHz) in [12]. This Γ corresponds to the *decay rate* or *linewidth* of this state.

The *transition probability* from the $7P_{\frac{3}{2}}$ state to the $6S_{\frac{1}{2}}$ ground state state (single channel) is defined by

$$\Gamma_{7P_{\frac{3}{2}} \rightsquigarrow 6S_{\frac{1}{2}}} = \frac{\omega_0^3}{3\pi\epsilon_0 \hbar c^3} \frac{2 \cdot \frac{1}{2} + 1}{2 \cdot \frac{3}{2} + 1} \left| \left\langle J = \tfrac{1}{2} \middle\| e\boldsymbol{r} \middle\| J' = \tfrac{3}{2} \right\rangle_{6S_{\frac{1}{2}} \to 7P_{\frac{3}{2}}} \right|^2 \tag{3.3}$$

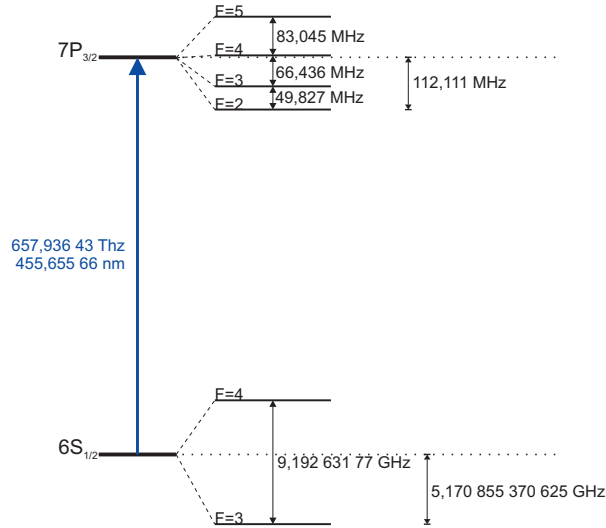All decay channels from the $7P_{\frac{3}{2}}$ state back to the ground state can be seen in Figure 3.2.

Figure 3.1: Level scheme of the $6S_{\frac{1}{2}} \to 7P_{\frac{3}{2}}$ transition with all hyperfine levels.
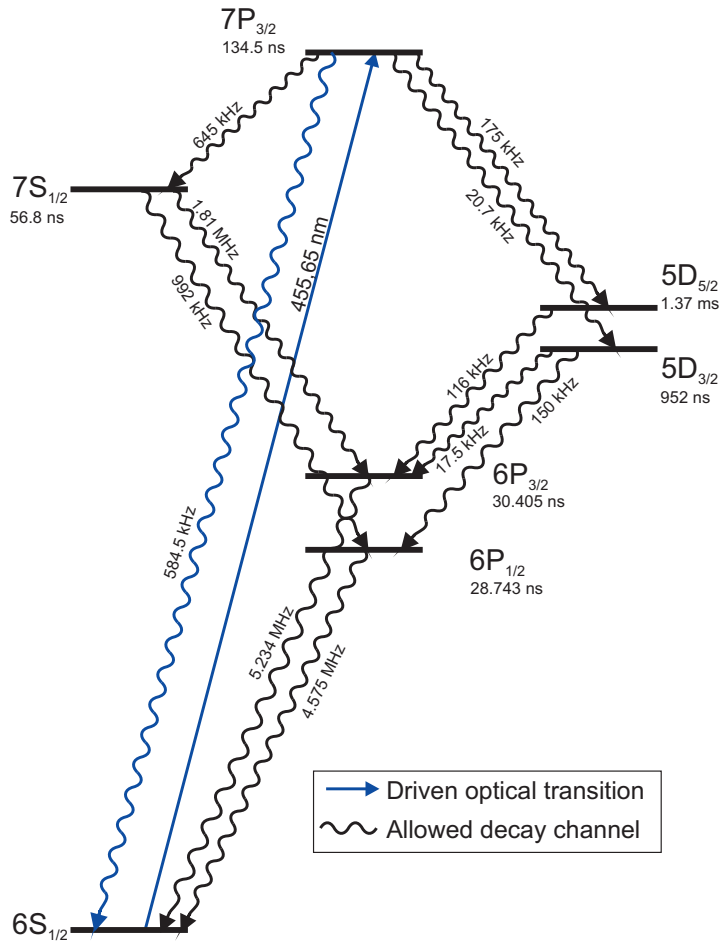

Figure 3.2: Level scheme of the $6S_{\frac{1}{2}} \to 7P_{\frac{3}{2}}$ transition with all allowed decay channels. The lifetime and transition probability values are taken from [4], [12] and [13] with the best precision available.
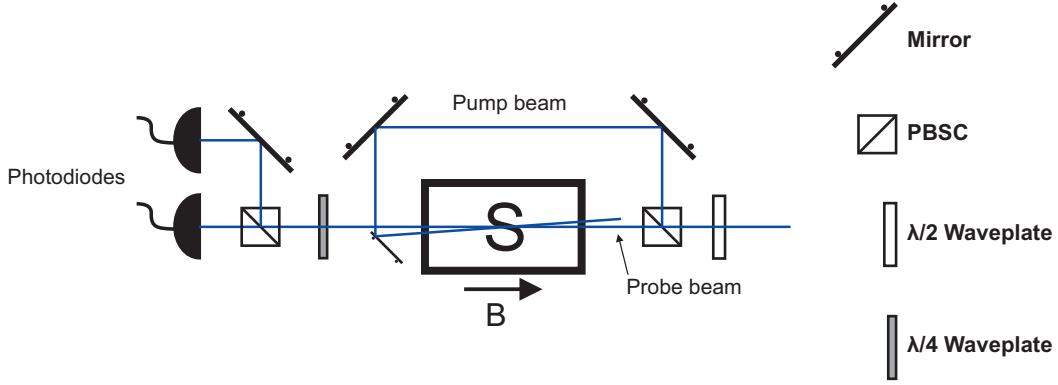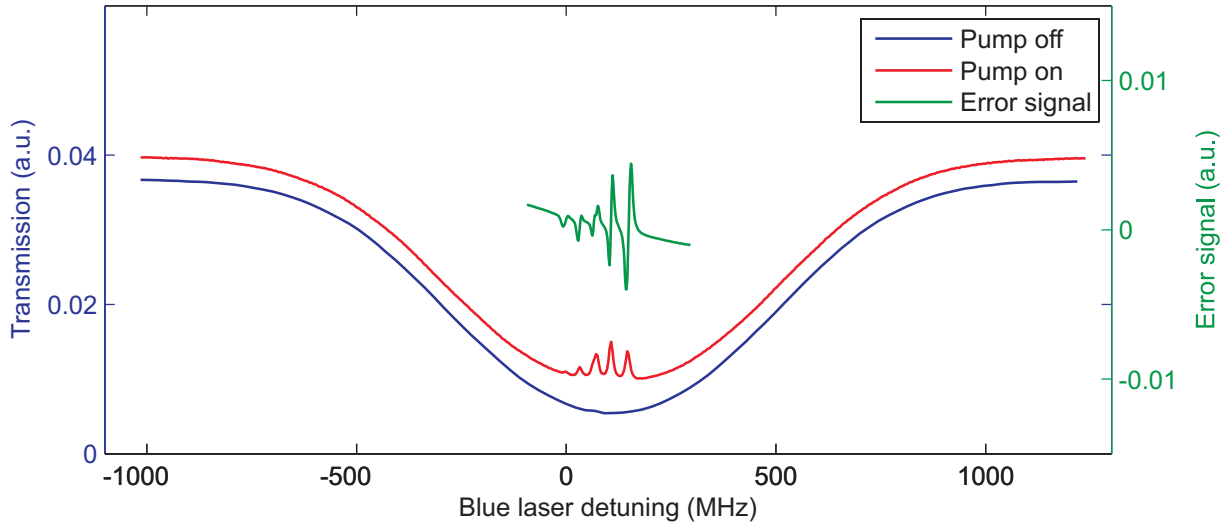
Figure 3.3: Schematic set-up of for DAVLL.

Figure 3.4: Absorption spectrum with and without pump beam, and error signal for the $6S_{\frac{1}{2}}(F = 4) \rightarrow 7P_{\frac{3}{2}}(F' = 3, 4, 5)$ transition.

3.2   455 nm laser set-up

3.2.1   Frequency locking procedure: DAVLL

We perform spectroscopy with the 455 nm laser in a thermal (approx. $60\,°C$) vapour cell of caesium atoms. At such a temperature, the atomic velocities are not negligible and the atoms experience the Doppler effect in their interaction with the light field. Hence, the pure spectroscopy signal is Doppler-broadened. In order to lock the 455 nm laser to the $6S_{\frac{1}{2}} \rightarrow 7P_{\frac{3}{2}}$ transition however, we need a Doppler-free signal. We chose the DAVLL (Dichroic Atomic Vapor Laser Lock) spectroscopy method with saturation spectroscopy in a magnetic field [14]. In the case of the D2-line of caesium, polarization spectroscopy is supposed to produce a better locking signal than the DAVLL method with saturation spectroscopy in a magnetic field. However, we tried both methods in our case and there was no significant improvement of the locking signal with polarization spectroscopy, so we used the DAVLL technique.

The set-up for the saturation spectroscopy is shown in Figure 3.3. The incoming laser beam is split with a half-wave plate and a PBSC (Polarizing Beam-Splitting Cube) into a strong pump
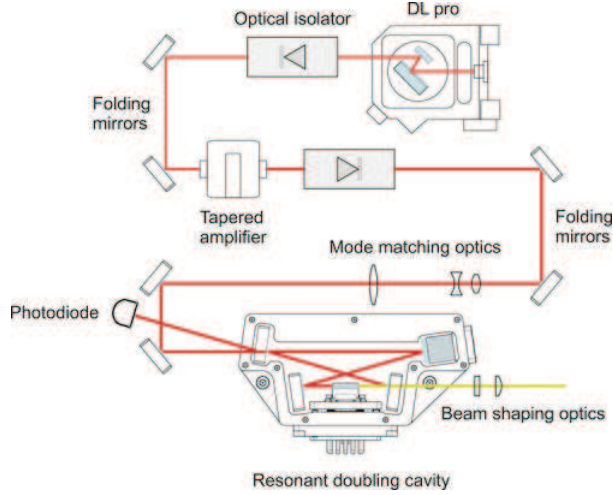
Figure 3.5: Inside configuration of the Toptica TA-SHG Pro laser (source: Toptica website).

beam and a weak probe beam, both linearly polarized. The probe beam passes directly through the spectroscopy cell to the detectors. The pump beam is overlapped with the probe beam in an almost counter-propagating way. The probe laser beam sees the whole Doppler distribution (see Figure 3.4). When the pump beam is on, both probe and pump beam are simultaneously resonant with the same velocity class when the laser is resonant to one single hyperfine transition. This velocity class is the class of atoms that are moving perpendicularly to the beam ($\vec{k} \cdot \vec{v} = 0$). In this case, the atoms are mainly driven by the strong pump beam, and the vapour becomes more transparent for the probe beam. This results in transmission peaks (Lamb-dips) at the position of the transitions and crossovers (see Figure 3.4).

If we apply a magnetic field parallel to the laser beams in the spectroscopy cell, the degeneracy of the hyperfine sublevels is lifted due to the Zeeman effect. Hence the σ^+ and σ^- components of the linearly polarized beams are not simultaneously resonant with the atoms. These two components are split using a quarter-wave plate and a PBSC, each being sent to one detector. The difference of these two signals gives the error signal (see Figure 3.4). This error signal is produced by a differential amplifier and sent to a Proportional-Integral-Derivative (PID) Controller. The locking signal generated by the PID Controller is fed back into the laser. Each Lamb-dip gives rise to one zero-crossing slope on the error signal, on which we can lock the laser.

3.2.2 Set-up

The laser system (Toptica TA-SHG Pro) consists of a tunable diode laser (External Cavity Diode Laser) seeding a tapered amplifier. The infrared beam of this tapered amplifier has a power of approx. 1 W after the optical isolator, is reshaped and coupled into a ring cavity, in which a non linear frequency doubling crystal is located (See Figure 3.5).

The output power of the frequency doubled light at 455 nm is approx. 220 mW. From this, we use approx. 5 mW for the frequency locking process. Before going into the DAVLL spectroscopy, the beam passes through two acousto-optical modulators (AOM) in double pass configuration (see Figure 3.6). The first AOM is adjusted such that the 1st order of the diffraction pattern is selected. The second AOM is adjusted such that the -1st order of the diffraction pattern is selected. The detuning of the beam used to perform the DAVLL spectroscopy with respect to the original laser beam is therefore twice the difference between the two AOM frequencies. This allows us to precisely set the laser detuning to one atomic resonance. The two main cases of interest are the resonant one (AOM frequencies: +200 MHz and -200 MHz) and the far detuned
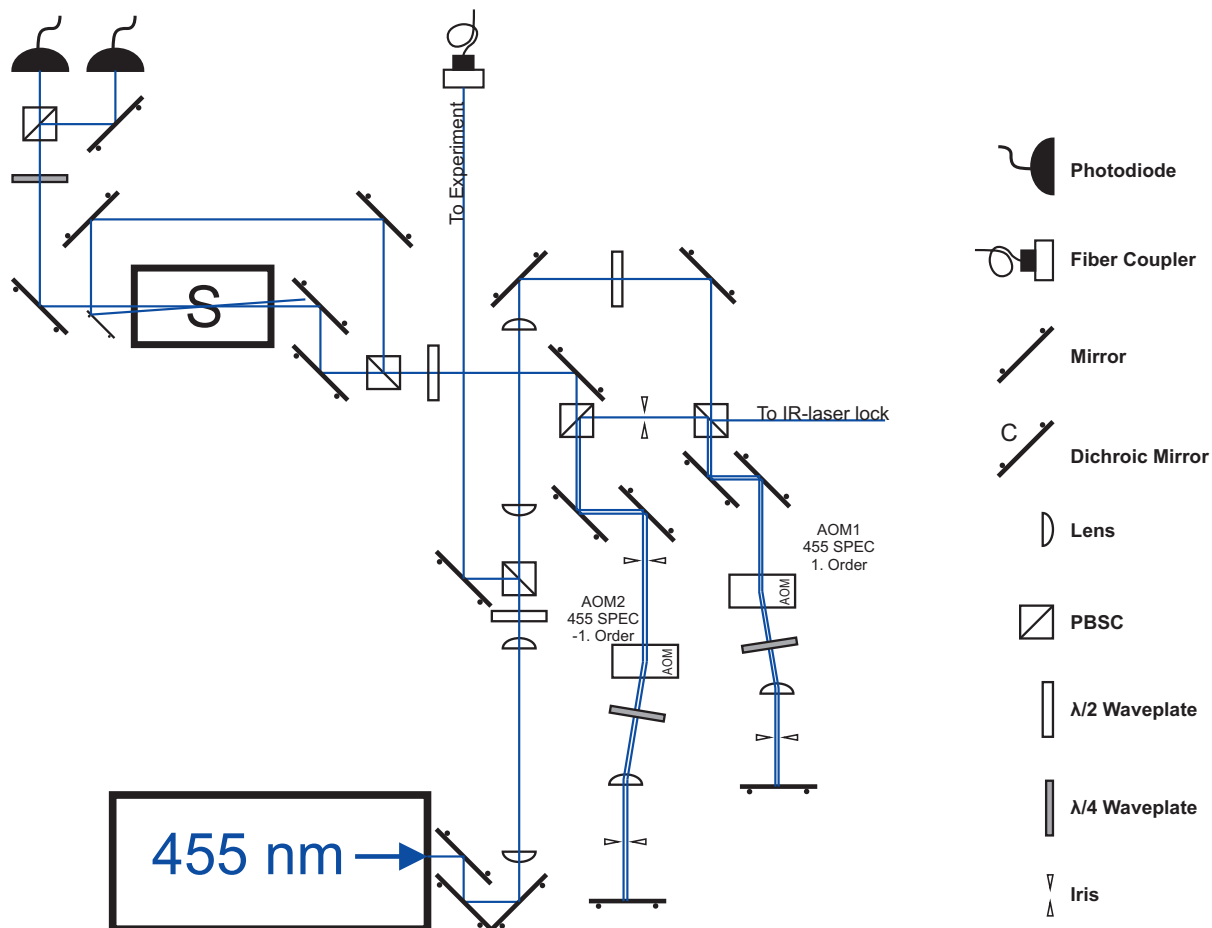
Figure 3.6: Set-up for locking the 455 nm laser.

one (AOM frequencies: +180 MHz and -220 MHz, detuning: -80 MHz). However, the optimal incoming beam angle to the AOM is strongly dependent on the AOM frequency. So, in order to have a similar efficiency after the two AOM double passes, we adjusted the AOMs on intermediate frequencies: +190 MHz and -210 MHz respectively. When the frequencies are back to +200 MHz and -200 MHz, we obtain an efficiency of around 30% after two double passes. The power of the beam going into the DAVLL spectroscopy is approx. 1 mW and its diameter is approx. 1 mm. We split this beam with the half-wave plate and the PBSC so that the probe beam has the lowest possible intensity (approx. 50 µW).

We used a home-made spectroscopy cell made out of quartz glass. The cell is 7.5 cm long and has a diameter of 30 mm. The magnetic field is generated by a a coil around the cell with 180 windings. The cell is heated with a heating foil to obtain sufficient optical thickness, and the cell windows have additional heaters using a resistor and copper plates to avoid condensation of caesium.

3.2.3 Saturation absorption and DAVLL spectroscopy measurements

We performed systematic measurements with the DAVLL spectroscopy set-up in order to optimize the locking procedure. The parameters that were optimized are the optical pump and probe powers and the magnetic field in the spectroscopy cell.
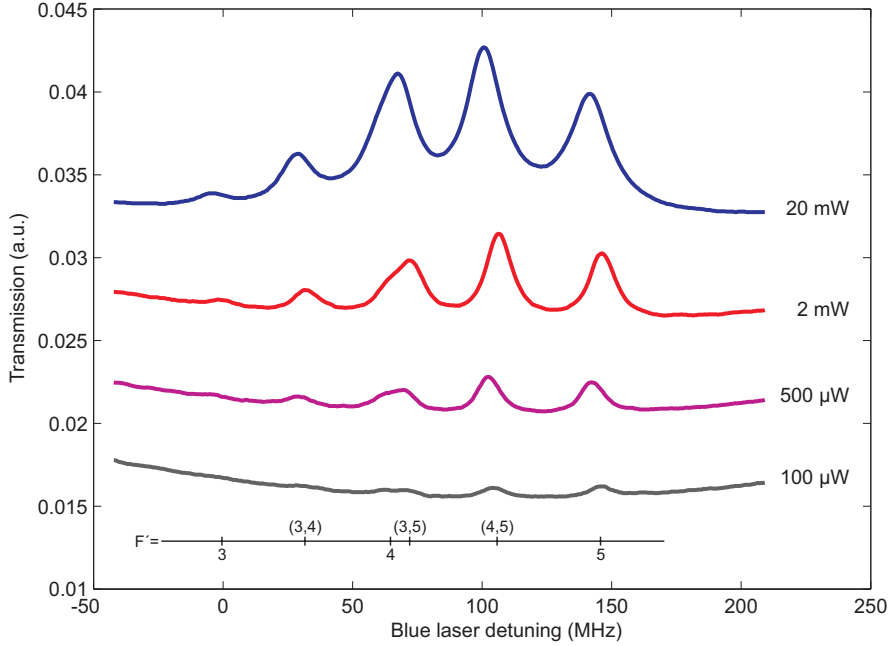
Figure 3.7: Transmission of the blue laser scanned at different pump powers (probe power: 2.5 µW, transition $F = 4 \to F' = 3, 4, 5$).

Saturation absorption spectroscopy optimization

We performed a scan over all the hyperfine transitions of the $6S_{\frac{1}{2}}(F = 4) \to 7P_{\frac{3}{2}}(F' = 3, 4, 5)$ transition for different pump and probe powers. The laser beam diameter was 1 mm.

One can see in Figure 3.7 the saturation absorption signal with the Lamb-dips for different pump powers. Our goal is to have significantly high Lamb-dips, without using too much power. One can see that at higher power (20 mW), the Lamb-dips get broadened, what we want to avoid for the DAVLL signal. So we chose a pump power of $\sim 1\,\mathrm{mW}$ since it is a satisfying trade-off between signal amplitude and used power.

We performed the same measurement for different probe powers. The results can be seen in Figure 3.8. 50 µW corresponds to the minimal achievable power 1 mW input power into the DAVLL set-up. We obtained 2.5 µW with attenuators before the cell. The signals were normalized to the same Doppler profile depth. The frequency shift of the two upper signals with respect to the first one is due to a drift of the laser. We could not see a significant effect of the different probe power on the relative height and width of the Lamb-dips. Therefore we chose a probe power of 50 µW to minimize possible saturation effects without having to attenuate the power of the probe beam before the cell.

DAVLL signal optimization

The error signal is obtained by taking the difference between the transmission of the σ^+ and σ^- components of the probe beam in the cell. Its shape depends on the strength of the magnetic field inside the cell, and therefore on the current applied to the coil. Figure 3.9 displays the error signal at different currents. The signal at 0 G applied magnetic field indicates the presence of stray magnetic fields, probably emerging from the optical isolators of our Toptica TA-SHG pro standing nearby and from the earth. We also notice that at 28 G applied magnetic field, the slopes become less steep and unclean, as a cause of the specific Zeeman coefficients to the ground and excited states. For an efficient locking we want to have slopes as steep as possible

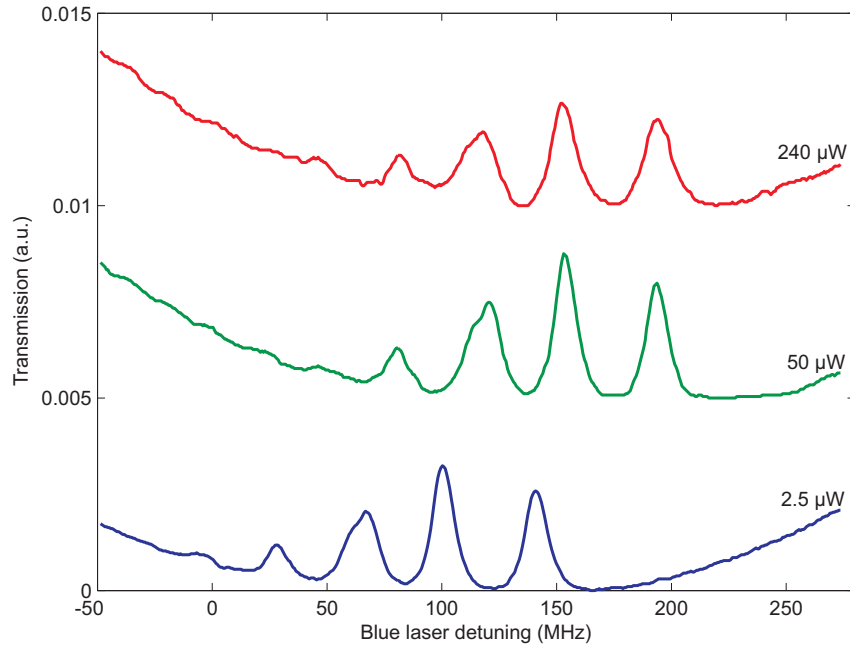Figure 3.8: Transmission of the blue laser scanned at different probe powers (pump power: ~ 1 mW, transition $F = 4 \rightarrow F' = 3, 4, 5$).
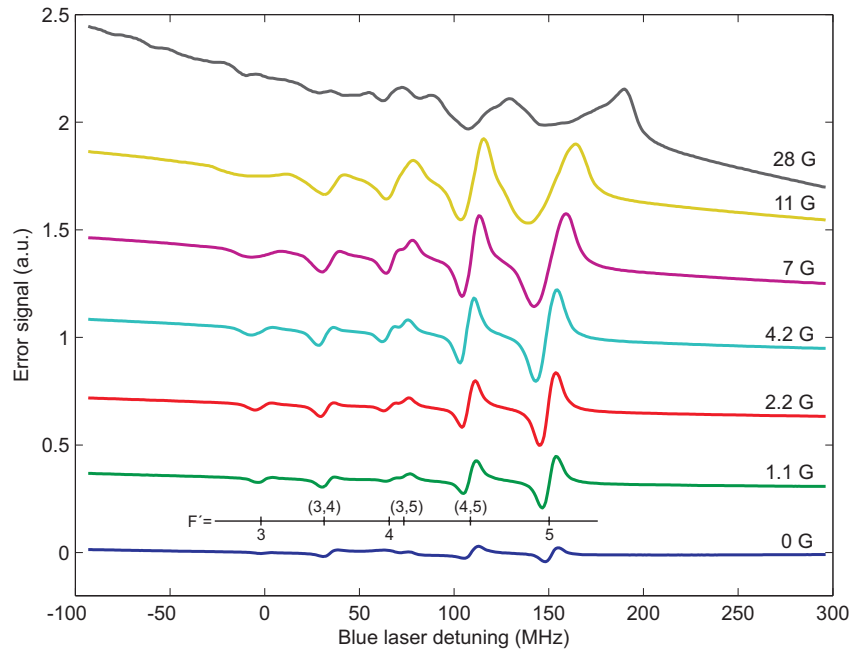

Figure 3.9: Error signal for different magnetic fields (transition $F = 4 \rightarrow F' = 3, 4, 5$).

and a large amplitude. Thus, we selected in the end a magnetic field of 4.2 G (current of 150 mA through the coil), as this signal appears to be a good trade-off between the two criteria.

3.3   Temperature measurements

The optical thickness of our 7.5 cm long cell for the $6S_{\frac{1}{2}} \rightarrow 7P_{\frac{3}{2}}$ transition at room temperature is relatively low (transmission reduced by approx. 5 % on resonance) compared to the D-line $(6S \rightarrow 6P)$, so we need to heat the cell up to get a significant signal. The heating was set to obtain a transmission reduced by approx. 60 %. on resonance (see Figure 3.12). However it is not possible to measure this temperature directly.

The temperature of the cell can be obtained by fitting the absorption spectrum. Along with the temperature, another important fitting parameter is the '2-level-like' saturation intensity. Because of the more complex nature of our system (several decay channels) compared to the D-line, we cannot estimate this saturation intensity in a straight forward manner using the 2-level formula. Although a fitting procedure on both the temperature and the saturation intensity simultaneously would be possible, we decided to go for a more robust approach using a 895 nm laser[1] driving the D1-line $6S_{\frac{1}{2}} \rightarrow 6P_{\frac{1}{2}}$. We first fitted an absorption spectrum of the 895 nm laser in a cell at room temperature to obtain a fitted value of the saturation intensity of the D1-line. With this value of the saturation intensity, we fitted the absorption spectrum of the 895 nm laser in the cell used for the 455 nm laser set-up to obtain a fitted value of the cell temperature. This allowed us to fit the absorption spectrum of the 455 nm laser with this value of the temperature and obtain a fitted value of the saturation intensity for the $6S_{\frac{1}{2}} \rightarrow 7P_{\frac{3}{2}}$ transition afterwards.

3.3.1   Fitting function

From equation 2.18, the absorption profile for the D1-line $(6S_{\frac{1}{2}}(F = 3, 4) \rightarrow 6P_{\frac{1}{2}}(F' = 3, 4))$ is given by the formula:

$$
\alpha(\delta, T) = n(T)\sigma_0 \frac{\pi\Gamma}{2} \sqrt{\frac{\ln 2}{\pi}} \frac{2}{\omega_D} \times \left(\frac{7}{16} \left(\frac{7}{12} e^{-4\ln 2(\frac{\delta - 4514.0354}{\omega_D})^2} + \frac{7}{4} e^{-4\ln 2(\frac{\delta - 5681.7154}{\omega_D})^2} \right) \right.
$$
$$
\left. + \frac{9}{16} \left(\frac{7}{4} e^{-4\ln 2(\frac{\delta + 4678.5964}{\omega_D})^2} + \frac{5}{4} e^{-4\ln 2(\frac{\delta + 3510.9164}{\omega_D})^2} \right) \right)
$$

(3.4)

The 7/16 and 9/16 express the probability of the atoms to be initially in the $F = 3$ or $F = 4$ hyperfine ground state. It is determined by the number of magnetic sublevels. The other fractional factors express the relative strengths of each hyperfine transition.

In the case of the $6S_{\frac{1}{2}} \rightarrow 7P_{\frac{3}{2}}$ transition, the formula yields:

$$
\alpha(\delta, T) = n(T)\sigma_0 \frac{\pi\Gamma}{2} \sqrt{\frac{\ln 2}{\pi}} \frac{2}{\omega_D}
$$
$$
\times \left(\frac{7}{16} \left(\frac{5}{6} e^{-4\ln 2(\frac{\delta - 5058.7446}{\omega_D})^2} + \frac{7}{8} e^{-4\ln 2(\frac{\delta - 5108.5716}{\omega_D})^2} + \frac{5}{8} e^{-4\ln 2(\frac{\delta - 5175.0076}{\omega_D})^2} \right) \right.
$$
$$
\left. + \frac{9}{16} \left(\frac{7}{24} e^{-4\ln 2(\frac{\delta + 4084.0602}{\omega_D})^2} + \frac{7}{8} e^{-4\ln 2(\frac{\delta + 4017.6241}{\omega_D})^2} + \frac{11}{6} e^{-4\ln 2(\frac{\delta + 3934.5791}{\omega_D})^2} \right) \right)
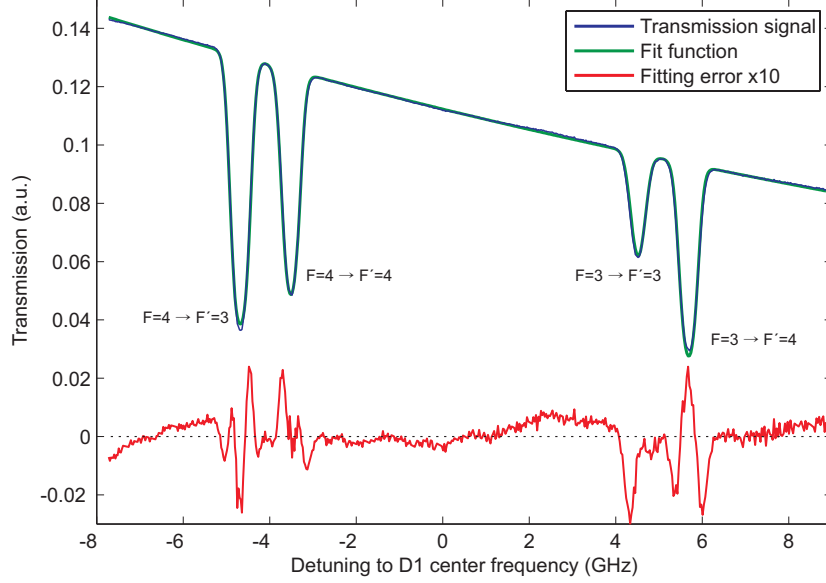$$

(3.5)

---

[1]Toptica DL100 pro design

Figure 3.10: Transmission signal of the D1-line ($6S_{\frac{1}{2}} \to 6P_{\frac{1}{2}}$), fitted function and fitting error taken in a 7.5 cm Cs cell at 20 °C.

In both formulas the positions of the hyperfine transitions are given in MHz relatively to the line centre, and $n(T)$ is the atomic density from equation 2.1.

We could fit the measured transmission profiles to the relative intensity defined by the Lambert-Beer law:

$$I_{rel} = \frac{I_{out}}{I_{in}} = e^{-\alpha d} \tag{3.6}$$

d being the cell length, with T and I_{sat} as fitting parameters, and allowing a non-linear[1] time to frequency scaling, a non-linear[1] light intensity[2] and a non-linear[1] offset.

3.3.2 Saturation intensity of the D1-line

We took an absorption spectrum of the D1-line at room-temperature (20 °C) in a similar cell to the one used in the previously described set-up. The laser beam was very weak (15 µW, intensity of approx. $1\,\mathrm{W/m^2}$) and therefore far from the power broadened regime. The signal was then fitted, keeping the temperature as a fixed parameter. The signal, the fitted function and the fitting error are shown in Figure 3.10. Note that the fitting error was magnified. The fitted value for the saturation intensity is $I_{sat} = 61.3\,\mathrm{W/m^2}$. The theoretical value calculated with the $\left\langle J = \frac{1}{2} \left\| e\boldsymbol{r} \right\| J' = \frac{1}{2} \right\rangle$ reduced dipole matrix element is $I_{sat} = 8.35\,\mathrm{W/m^2}$. The difference in the two values accounts for pumping effects within the manifold of the bright ground state, pumping effects in the dark state in the dark ground state, and its compensation by the transit time of the atoms through the beam.

Leaving also the temperature free as a fitting parameter results in a higher value than the expected one. This basically means that the Doppler profiles are broader than the ones expected from theory. Our home-made spectroscopy cell was filled under a background gas pressure of approx. 10^{-6} mbar. The vapour pressure of caesium at room temperature is also on the order of 10^{-6} mbar. So we could expect that pressure broadening is responsible for this deviation, and our results are therefore not inherently inconsistent.

---

[1] 2nd order polynomial
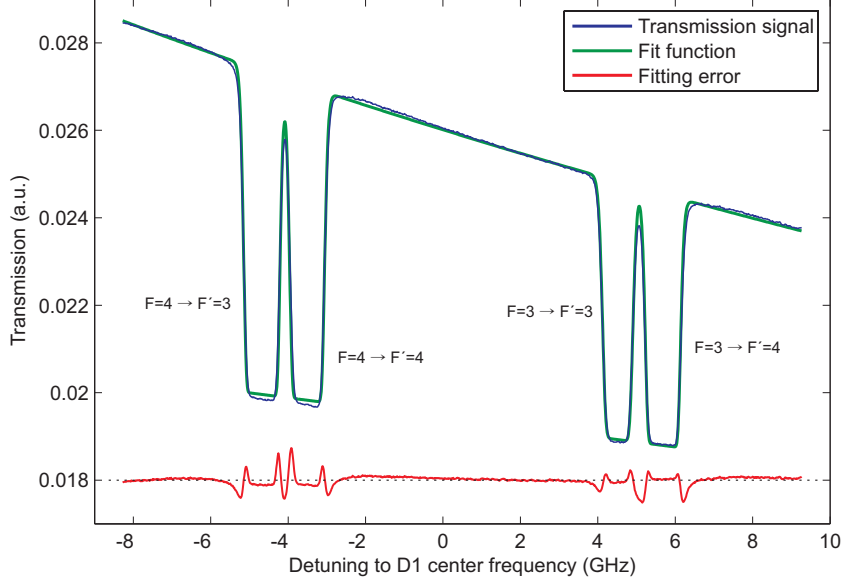[2] accounting for the feed-forward system in the lasers

Figure 3.11: Transmission signal of the D1-line ($6S_{\frac{1}{2}} \rightarrow 6P_{\frac{1}{2}}$), fitted function and fitting error taken in the 7.5 cm Cs cell used in the blue laser set-up. The fitted temperature is 58 °C.

3.3.3 Temperature of the "blue" spectroscopy cell

With the previously determined value for the saturation intensity of the D1-line of caesium we could take a reference absorption spectrum of the D1-line in the same cell used in the blue laser set-up. Again we work in the weak intensity regime (approx. $0.8 \, \mathrm{W/m^2}$). This time we left the saturation intensity we identified before as a fixed parameter, and the temperature was left as free fitting parameter. The signal and the fitting results are shown in Figure 3.11. The temperature we obtain from the fitting is 58 °C which seems to be a realistic value.

The fitting error was rather substantial. At such a temperature, our caesium cell is expected to be optically thick. The bottoms of the transmission dips should therefore coincide with the zero transmission level. As one can see in Figure 3.11, the bottoms of the transmission dips are flat and inclined instead of coinciding with the zero transmission level. This might be caused by another mode coexisting in the laser. We added a polynomial offset to try to compensate for this effect.

If we also leave the saturation intensity as a free fitting parameter, the fitted temperature is 119 °C. This results in smaller fitting errors but with an unlikely temperature. The fact that this unlikely temperature is higher than expected could be partly explained by the presence of pressure broadening.

3.3.4 Absorption of the blue laser on the $6S \rightarrow 7P$ transition

A similar measurement was then realized with the blue laser on the $6S_{\frac{1}{2}} \rightarrow 7P_{\frac{3}{2}}$ transition. The signal was first fitted with a fixed temperature of 58 °C. The results are shown in Figure 3.12. The fit is rather good, since the error mainly emerges from the laser intensity which has a peculiar behaviour that could not be fitted perfectly by our function, as one can see with the off resonant signal in Figure 3.12. The saturation intensity obtained from the fitting for the $6S_{\frac{1}{2}} \rightarrow 7P_{\frac{3}{2}}$ transition with $T = 58 \, ^{\circ}\mathrm{C}$ is $I_{sat} = 424 \, \mathrm{W/m^2}$. If both the saturation intensity and the cell temperature are left as free parameters, they are fitted to $T = 52 \, ^{\circ}\mathrm{C}$ and $I_{sat} = 261 \, \mathrm{W/m^2}$, in which the fitting error is only slightly improved.
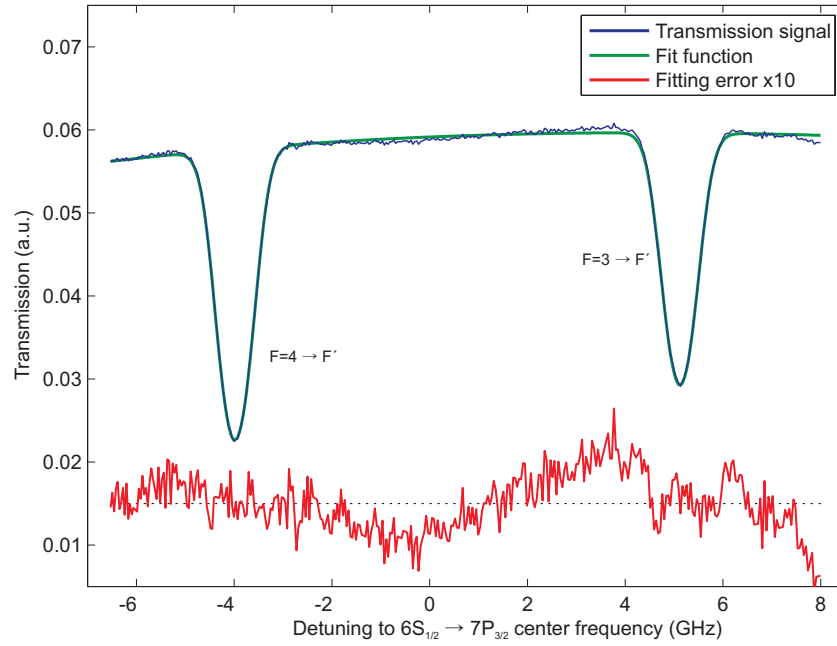
Figure 3.12: Transmission signal of the blue laser, fitted function and fitting error taken in the blue laser set-up for $T = 58\,^{\circ}\mathrm{C}$.

So the temperature of the spectroscopy cell used to lock the 455 nm laser was determined to be around $58\,^{\circ}\mathrm{C}$ by the fitting of the absorption spectrum. These fittings also provided rough estimates for the *effective* saturation intensities of the D1-line and the $6S_{\frac{1}{2}} \rightarrow 7P_{\frac{3}{2}}$ transition. Such values could be used to calculate the parameters of effective two-level models of these lines.

Chapter 4

A new way to the Rydberg states of caesium

The excitation scheme to Rydberg states that was chosen for this project differs slightly from previous approaches, e.g. with rubidium. The excitation scheme, its differences to previous approaches and the motivation for using this new scheme are described in the first section. Preliminary simulations showed that as in the case of rubidium one expects to observe electromagnetically induced transparency (EIT). The experimental set-up was designed for such measurements and is described in the second section. However the experimental results reported in the third section exhibit a peculiar behaviour not entirely understood by the present theory. The analysis and interpretations of these results will be performed in the fourth section by means of comparison to other works and analysis of possible unwanted effects.

4.1 The level scheme

Most experiments involving Rydberg states of alkali metals were performed on cold atoms where the slowing and trapping processes happen with the D2-line (if the ground state has n as principal quantum number, the D2-line is the $nS_{\frac{1}{2}} \rightarrow nP_{\frac{3}{2}}$ transition). Therefore the same laser system can be used for the first excitation step.

In the case of rubidium, the usual excitation scheme is the two-photon-transition $5S_{\frac{1}{2}} \rightarrow 5P_{\frac{3}{2}} \rightarrow nS, nD$ [15]. The same scheme has been used with thermal rubidium atoms in our group ([2],
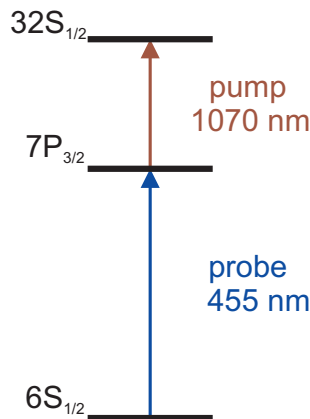

Figure 4.1: Level scheme of the considered three-level system to the $32S$ Rydberg state.

[3]). In the case of caesium, Rydberg excitation have been performed with the similar scheme $6S_{\frac{1}{2}} \to 6P_{\frac{3}{2}} \to nS, nD$ [16] and with the three-photon-transition scheme $6S_{\frac{1}{2}} \to 6P_{\frac{3}{2}} \to 7S_{\frac{1}{2}} \to nP$ on ultracold caesium atoms [17].

The excitation scheme that was chosen in our case can be seen in Figure 4.1. The $6S_{\frac{1}{2}} \to 7P_{\frac{3}{2}}$ transition is the first excitation step, driven by the 455 nm laser system described in the previous chapter. The Rydberg transition is the $7P_{\frac{3}{2}} \to nS, nD$. It is driven by a laser around 1070 nm, slightly depending on the principal quantum number of the chosen Rydberg state.

The dipole matrix element of the upper transition has been calculated for the $32S$ state using the method from [15] adapted to caesium. The wave functions are computed with the Numerov method and the dipole matrix elements are then calculated by integration. We obtain:

$$\left\langle J = \tfrac{3}{2} \middle\| e\boldsymbol{r} \middle\| J' = \tfrac{1}{2} \right\rangle_{7P_{\frac{3}{2}} \to 32S_{\frac{1}{2}}} = 3.06 \times 10^{-31} \, \mathrm{C \cdot m} \tag{4.1}$$

As a comparison, the value given by this method for the $6S_{\frac{1}{2}} \to 7P_{\frac{3}{2}}$ transition has a relative error of 6.3% to the experimental value from section 3.1. Since the computation of the wave function with the Numerov method improves drastically with the principal quantum number, one can assume that the above value is reasonably good.

The lifetime of the $32S$ Rydberg state was measured and calculated in [16] to be approx. $\tau_{32S} = 27 \, \mu\mathrm{s}$. This excitation scheme presents some advantages in comparison to the $5S_{\frac{1}{2}} \to 5P_{\frac{3}{2}} \to nL$ scheme in thermal rubidium. From a fundamental point of view, the dipole matrix element to the Rydberg state is larger than in the case of rubidium. Indeed caesium has one more inner electron shell than rubidium, so the similar states (e.g. $6P_{\frac{3}{2}}$ in Cs and $5P_{\frac{3}{2}}$ in Rb) are further away from the core in caesium than in rubidium, and the intermediate that we chose has a larger principal quantum number, which contributes to a larger overlap with the Rydberg state, and therefore to a larger dipole matrix element. This allows to have larger Rabi frequencies on the upper transition. From the technical point of view, the upper transition is at a wavelength of 1070 nm, which can be easily amplified by an ytterbium-doped fibre amplifier up to 15 W of optical power. A Pockels-cell can afterwards be used to produce pulses, in a much easier way than in a previous experiment [3]. Both these differences are interesting in the prospect of observing and utilizing fast (Gigahertz) Rabi oscillations thermal vapours.

The other difference to the rubidium case is the inverted ratio of the two wavenumbers of the two-photon-transition. This has an implication on the averaging process over the whole Doppler-distribution.

The chosen excitation scheme is basically a three-level system in a ladder configuration. EIT is expected from the simulations for such a system with the first transition being driven by a weak probe and the upper transition being driven by a strong coupling, independently of the difference of the wavenumbers.

4.2 Experimental set-up

The initial goal of the set-up was to measure EIT, in order to be able to implement a frequency locking procedure for the laser driving the upper transition afterwards.

The laser set-up described in section 3.2 is used for the first transition of the ladder system. An additional commercial diode laser drives the upper transition. The second laser (Toptica DL100 pro design) is a tunable diode laser (External Cavity Diode Laser) at 1070 nm. The output power after the optical isolator is approx. 110 mW. The set-up can be seen in Figure 4.2. The incoming laser beam at 455 nm passes through two AOMs in double pass configuration in the exact same way as described in section 3.2. These AOMs are also adjusted with a total detuning of −40 MHz. Once again, the purpose of these AOMs is to detune the laser beams without any
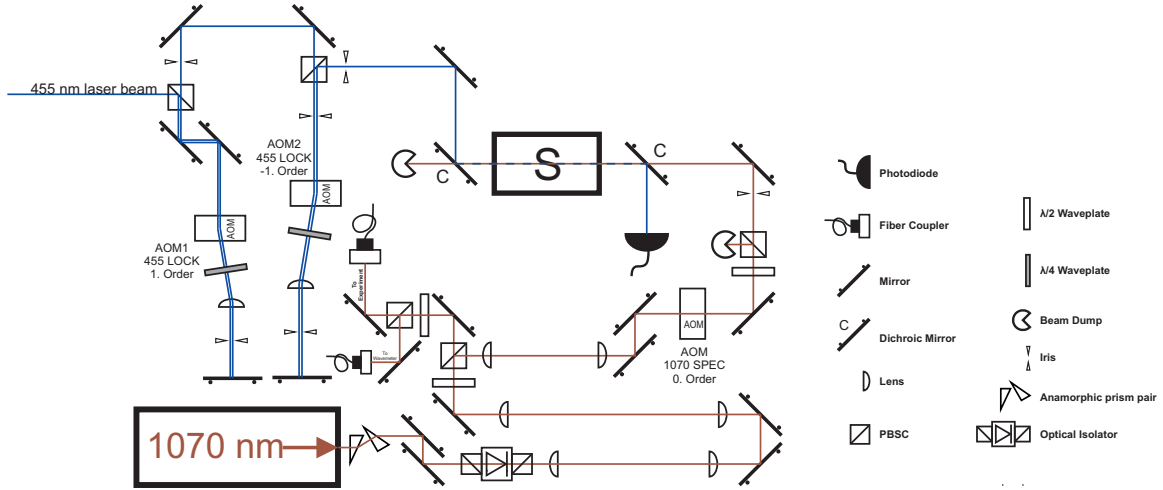
Figure 4.2: Set-up for the spectroscopy on Rydberg states.

restrictions. In this case, if the the AOMs detune the incoming frequency-locked blue beam, a non-zero velocity class ($\vec{k} \cdot \vec{v} \neq 0$) is selected and when the Rydberg laser is resonant, it is actually detuned from the zero velocity class ($\vec{k} \cdot \vec{v} = 0$). Overall, the four AOMs from the two set-ups allow to select the detuning of each beam to the zero velocity class independently. The blue beam is afterwards sent through the spectroscopy cell which is identical to the one described in section 3.2.

The beam of the 1070 nm laser is reshaped and collimated using an anamorphic prism pair and two telescopes to achieve a $\frac{1}{e^2}$ waist of 2 mm. We then use half-wave plates and PBSCs to split the beam into three beams: two of them are coupled into optical fibres to a wavemetre and to other experiments, and the third beam is used for our set-up. This beam needs to be reshaped afterwards to a waist of 1 mm to match the aperture of the chopping AOM that will be used for the amplitude modulation.

We use the amplitude modulation technique to enhance the signal-to-noise ratio by modulating the intensity of the 1070 nm pump beam. We select the 0th order beam of the Bragg diffraction for the experiment. The RF power is then chopped with 20 kHz and the measured signal is demodulated by an lock-in amplifier.

The modulated beam passes through a half-wave plate and a PBSC to choose the power of the beam in the experiment. Both the blue and infrared (IR) laser beams are overlapped in the spectroscopy cell in a counter-propagating configuration using a dichroic mirror. Another dichroic mirror separates the blue beam after the cell to be analysed by a photodiode. Both beams are linearly polarized.

For some of the measurements, this set-up was modified to have the beams focused instead of collimated in the cell, or to have the beams overlapped in a co-propagating configuration.

4.3 Experimental results

All measurements presented below were performed with the following excitation scheme:
$6S_{\frac{1}{2}}(F = 4) \rightarrow 7P_{\frac{3}{2}}(F' = 3, 4, 5) \rightarrow 32S$
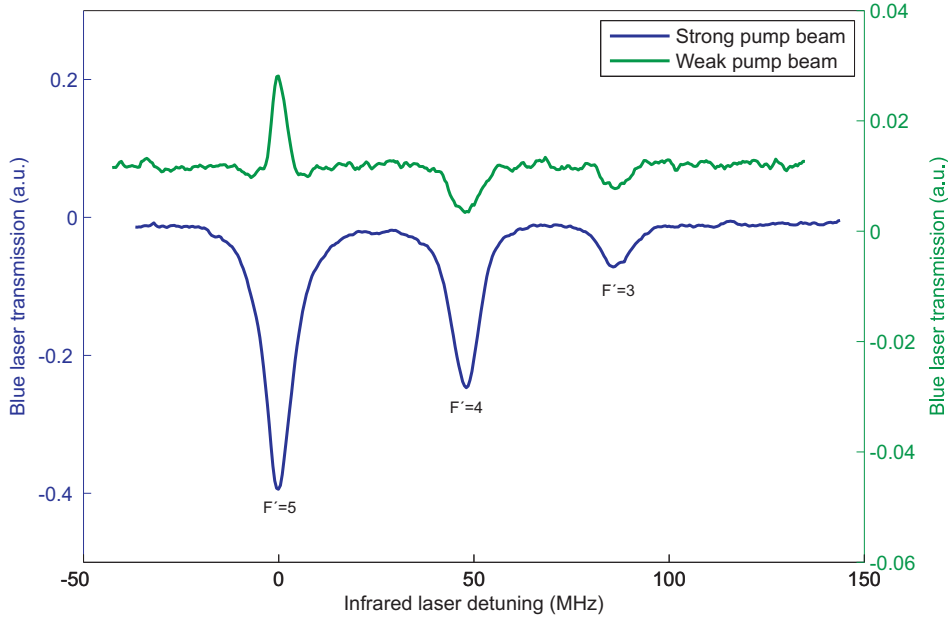Experiments from the other hyperfine ground state $6S_{\frac{1}{2}}(F = 3)$ produced similar results.

Figure 4.3: Blue laser transmission signal with the infrared laser being scanned. The beams were focused at $100\,\mu$m. The probe beam was weak (power of $24\,\mu$W, intensity of approx. $10^3\,\mathrm{W/m^2}$). The blue curve represents the spectrum with a strong pump beam (power of 95 mW (maximum available), intensity of approx. $10^8\,\mathrm{W/m^2}$). The green curve represents the spectrum with a weaker pump beam (power of $440\,\mu$W, intensity of approx. $10^5\,\mathrm{W/m^2}$). Note that the two y-axes are scaled differently. The spacing between these transmission dips is consistent with the hyperfine splitting of the intermediate state.

4.3.1 Observation of enhanced absorption

The very first measurements were performed with the laser beams focused into the cell (waist of $100\,\mu$m) in order to achieve larger peak Rabi frequencies and by this a bigger signal.

Surprisingly in our first try, we observed dips in the blue laser transmission instead of the expected peaks with a strong pump beam and a weak probe beam. When we started to change the pump intensity we were also able to observe a peak arising for the $F' = 5$ hyperfine intermediate state. The two extreme cases of strong and weak pump intensity are shown in Figure 4.3. One can see three clean transmission dips with a strong pump beam, and with a weak probe beam for a small transmission peak $F' = 5$ and transmission dips for $F' = 3, 4$. The signal was averaged over 256 traces in the weak pump beam case.

Intensity dependence of the system

We performed systematic measurements for different pump and probe intensities in order to understand the behaviour of the enhanced absorption and of the EIT that we observe.

Working with focused beams is interesting because the peak intensity is higher. It is a way to achieve higher Rabi frequencies, or to save optical power for other applications. However focused beams induce a broadening as the intensity is not constant and the observed signal is an integration over the beam path in the spectroscopy cell. In order to understand the behaviour of our system, it is preferential to have a single intensity/Rabi frequency over the whole cell. So the beams were not focused for these measurements.

For the measurements, signals were taken systematically for different combinations of probe (blue) and pump (IR) intensities following a rectangular pattern . The measurements were done

for co- and counter-propagating beams. The blue beam diameter was 1 mm. The infrared beam diameter was approx. 1.5 mm in the counter-propagating case and approx. 2 mm in the co-propagating case. The corresponding data sets are shown in the Figures 4.4 to 4.11. On each Figure there is one set of measured spectra for one of the intensities kept constant, in the co- or counter-propagating case. Each signal is an average over 32 traces. Note that the Figures 4.10, 4.11 and 4.8 are split in two parts. This is due to the fact that a change of parameters on the photodiode and on the lock-in amplifier had to be made in order to keep a good detection signal, without the possibility to rescale by comparing the signals before and after the change.

Weak probe beam For a weak probe beam, in the case of the counter-propagating beams (Figure 4.4), for the $F' = 5$ hyperfine intermediate state, the EIT peak amplitude grows first as we increase the pump intensity before shrinking as a broader transmission dip grows. The transition seems to occur for a pump intensity of around $30\,\mathrm{kW/m^2}$, and the signal shows a dispersive behaviour during the transition. For co-propagating beams (Figure 4.5) the evolution of the EIT peak is similar though we do not see an transmission dip, as we could not achieve as much pump intensity as with counter-propagating beams ($19\,\mathrm{kW/m^2}$ against $47\,\mathrm{W/m^2}$). We could however observe that the peak takes a dispersive shape as the pump intensity is increased, similarly to the situation of the counter-propagating beams.
In both cases for the two other intermediate states $F' = 3$ and $F' = 4$ we see transmission dips. Their amplitude decrease as we turn the pump intensity down before becoming undistinguishable.

Strong probe beam Here both cases of counter- and co-propagating beams (Figures 4.6 and 4.7 respectively) are quite similar. There is an EIT peak for each hyperfine intermediate state whose amplitude decreases as we turn the pump intensity down. We also notice that for high pump intensities, this peak seems to sit on top of a smaller and broader transmission dip.

Weak pump beam For a weak pump beam, only the features from the $F' = 5$ hyperfine intermediate state are clearly visible. In both cases of counter- and co-propagating beams (Figures 4.8 and 4.9 respectively), there is an EIT peak that gets broader and bigger with the probe intensity. The position at which the features from the $F' = 3$ and $F' = 4$ states should occur are however shown.

Strong pump beam In the strong pump and counter-propagating beams case (Figure 4.10) for the $F' = 3$ and $F' = 4$ hyperfine intermediate states, we first see an transmission dip growing as we increase the probe intensity. This dip then gets overcome by an faster growing EIT peak as we increase the probe intensity further. For $F' = 5$, This transition also happens, but the signal takes a dispersive shape during the transition, instead of being a growing peak sitting on top of a dip. We can extract from the data rough values for the probe beam intensity at which the transitions are happening: for $F' = 5$ at $100\,\mathrm{W/m^2}$, for $F' = 4$ at $1\,\mathrm{kW/m^2}$ and for $F' = 3$ at $6\,\mathrm{kW/m^2}$. For co-propagating beams (Figure 4.11), the same is occurring with $F' = 3$ and $F' = 4$ (at $200\,\mathrm{W/m^2}$). For $F' = 5$, we only see that the EIT peak takes a dispersive shape for small probe intensities, once again as the achievable pump intensity was smaller.
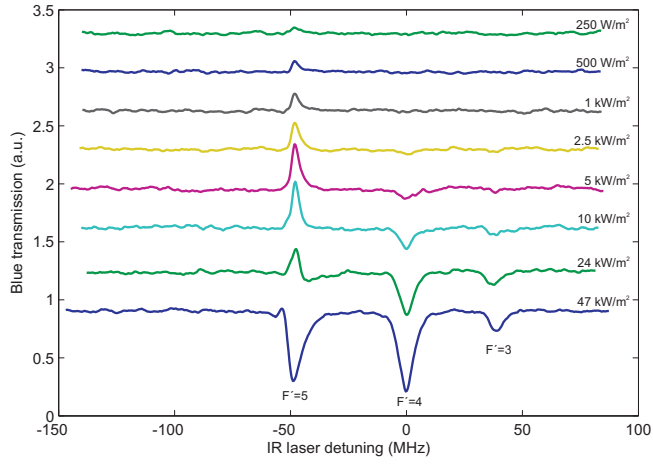
Figure 4.4: Blue laser transmission signal for different pump beam intensities with *counter-propagating* beams. The probe beam intensity is $25\,\mathrm{W/m^2}$.

Figure 4.5: Blue laser transmission signal for different pump beam intensities with *co-propagating* beams. The probe beam intensity is $25\,\mathrm{W/m^2}$.

Figure 4.6: Blue laser transmission signal for different pump beam intensities with *counter-propagating* beams. The probe beam intensity is $6.4\,\text{kW/m}^2$.
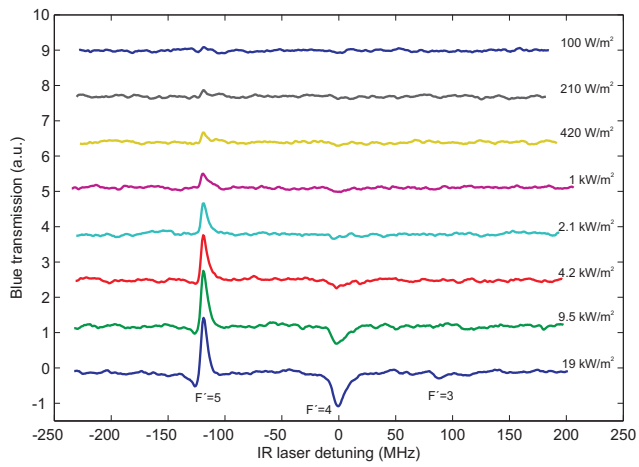

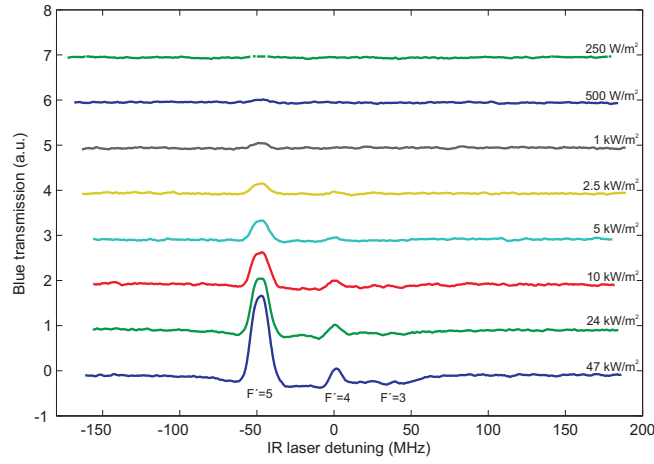Figure 4.7: Blue laser transmission signal for different pump beam intensities with *co-propagating* beams. The probe beam intensity is $6.4\,\text{kW/m}^2$.

Figure 4.8: Blue laser transmission signal for different probe beam intensities with *counter-propagating* beams. The pump beam intensity is $1\,\mathrm{kW/m^2}$.

Figure 4.9: Blue laser transmission signal for different probe beam intensities with *co-propagating* beams. The pump beam intensity is $420\,\mathrm{W/m^2}$.

Figure 4.10: Blue laser transmission signal for different probe beam intensities with *counter-propagating* beams. The pump beam intensity is $48\,\mathrm{kW/m^2}$.
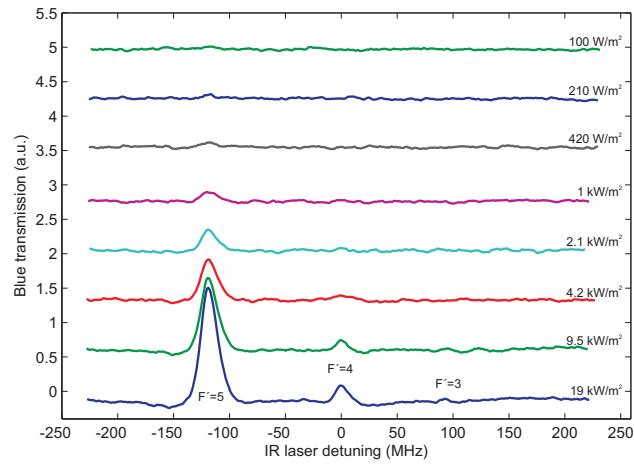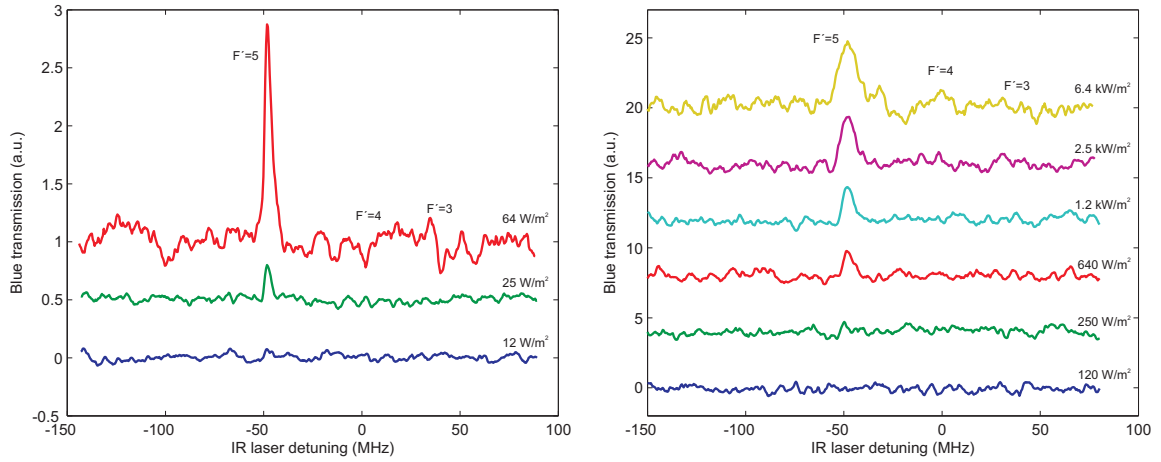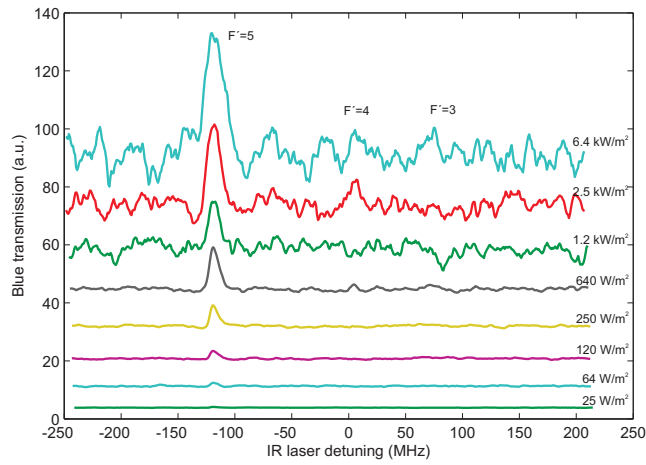

Figure 4.11: Blue laser transmission signal for different probe beam intensities with *co-propagating* beams. The pump beam intensity is $19\,\mathrm{kW/m^2}$.
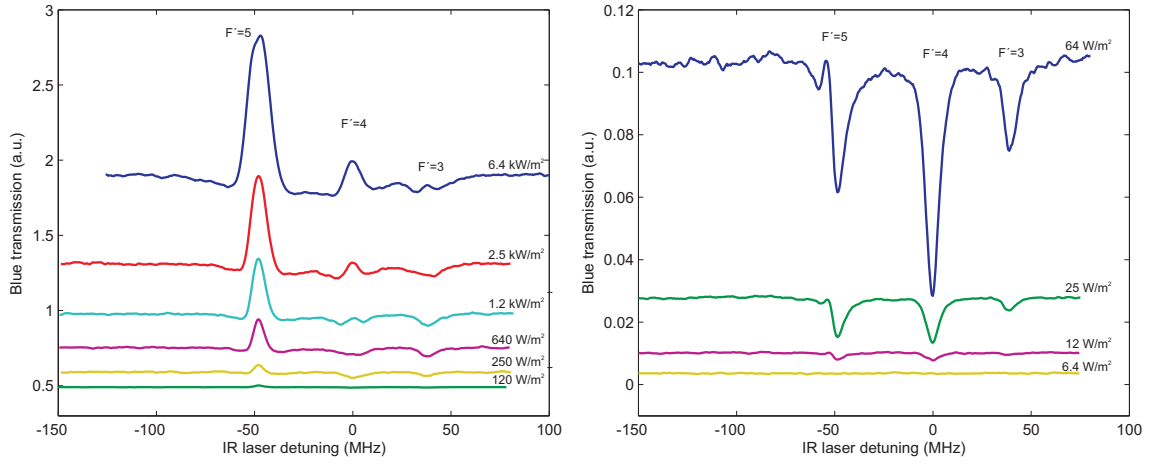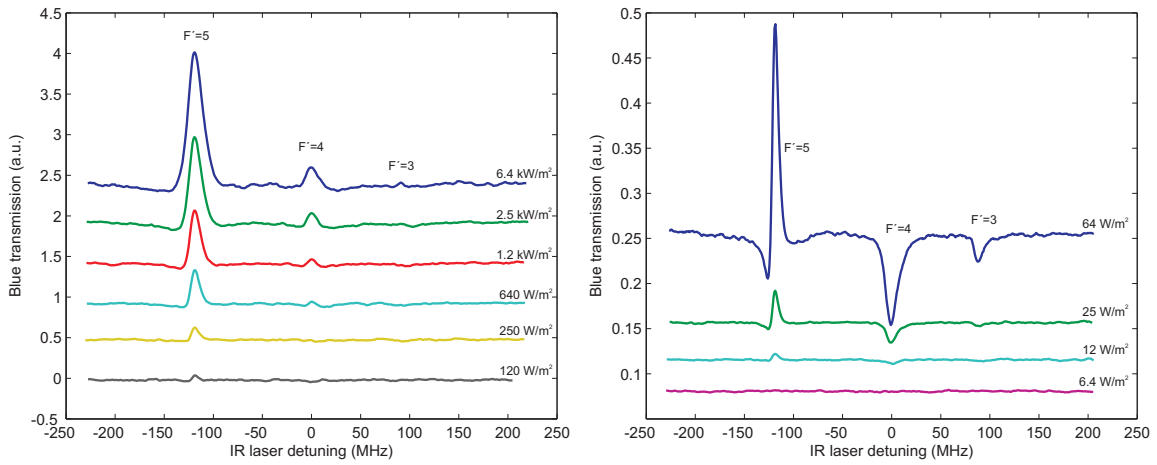
A overview of these results for $F' = 4, 5$ with co- and counter-propagating beams is presented in Figure 4.12. We notice that the results for counter- and co-propagating beams are perfectly compatible regarding the prevalence of EIT or enhanced absorption.

Now the information concerning the transmission and absorption peaks that we can extract from these measurements is the following:

- There are two phenomena competing, the enhanced transmission and the enhanced absorption.

- At constant blue (probe) intensity, increasing the IR intensity leads the absorption to take over the EIT.

- At constant IR (pump) intensity, a small blue intensity leads to enhanced absorption and as we increase the blue intensity, EIT takes over.

- There seems to be a minimal blue intensity below which it is not possible to observe a transmission peak (see left side of Figure 4.12(b)).

- The transition between enhanced absorption and the enhanced transmission shows a different behaviour between the hyperfine intermediate states $F' = 5$ and $F' = 3, 4$. For $F' = 5$, a dispersive behaviour is observed whereas for $F' = 3, 4$ we observe a peak and a dip that are competing.

Starting from this, we will now try to explain the presence of unexpected absorption peaks and their relative behaviour to the transmission peaks.

(a) $F' = 5$

(b) $F' = 4$
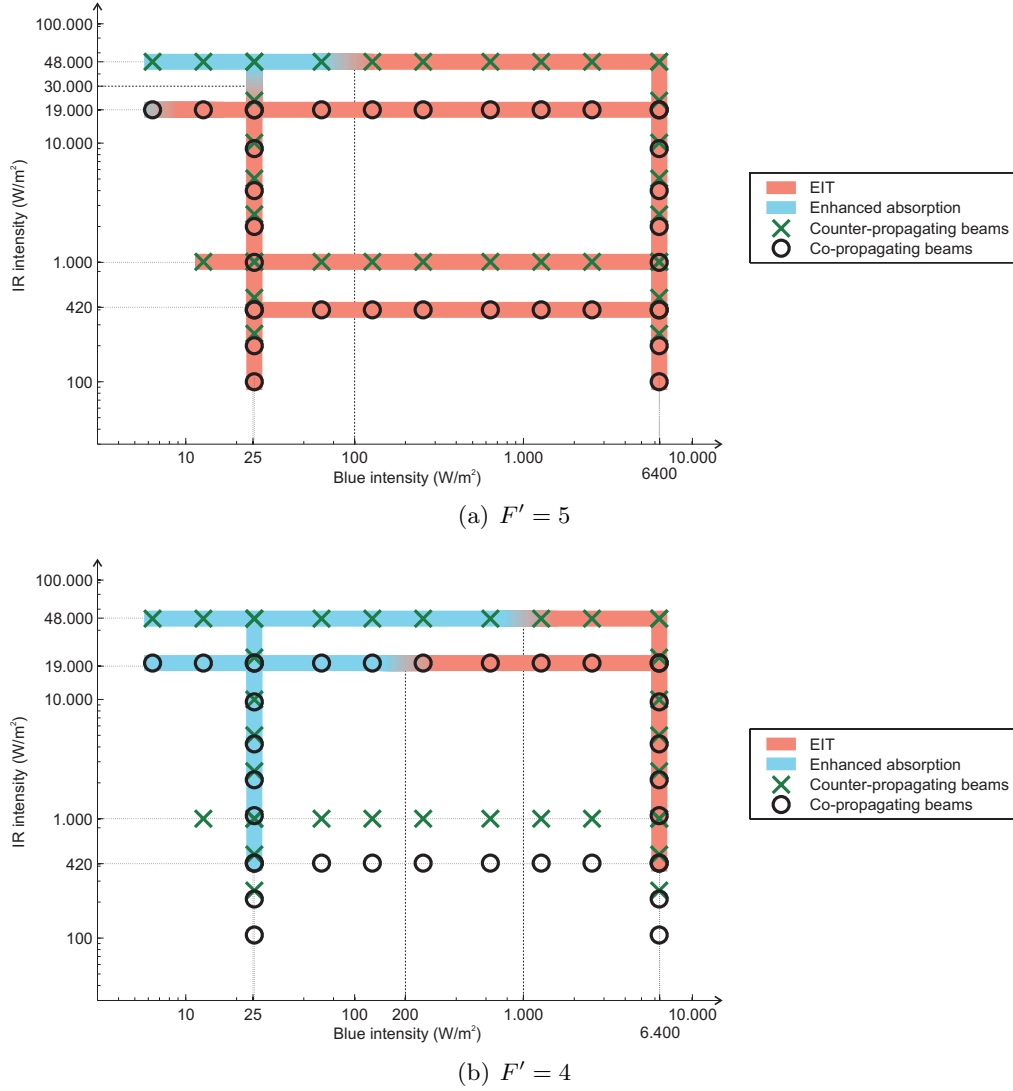
Figure 4.12: Blue and infrared intensity dependence of the EIT/absorption for the $6S_{\frac{1}{2}}(F = 4) \rightarrow 7P_{\frac{3}{2}}(F' = 4, 5) \rightarrow 32S$ excitation scheme. The measurement points are shown as green cross for counter-propagating beams and black circles for co-propagating beams. (a) is for $F' = 5$ and (b) for $F' = 4$. The thick coloured line represents the prevailing observed effect. The colour cross-fading represents the rough transition interval between the two effects. No thick line is drawn in case the effect is not distinguishable.

4.4 Analysis and interpretation

Enhanced absorption of the blue laser is not expected from theoretical simulations of ladder-type three-level systems like ours. However, it has been reported in other works on three-level ladder-type systems that one can observe absorption peaks ([18] and [19]). We will see that the explanation of these results relies on the fact that perfect three-level ladder-type systems rarely exist, and that the theoretical treatment of Moon et al. [19] can apply to our system.

4.4.1 Three-level ladder-type systems in the reality

Hayashi et al. have conducted studies of electromagnetically induced transparency in hot sodium atomic vapours [18]. Four different ladder type systems in sodium were investigated. For the $3S_{\frac{1}{2}} \rightarrow 3P_{\frac{1}{2},\frac{3}{2}} \rightarrow 5S_{\frac{1}{2}}$ system, absorption peaks and even transitions from absorption peaks to transmission peaks were observed. They interpreted the enhanced absorption to arise from two-photon absorption (TPA), but they were not able to explain the transitions between the two regimes.

Moon et al. have conducted extensive studies of three-level ladder-type systems in rubidium atoms ([20], [21], [19]). In the $5S_{\frac{1}{2}} \rightarrow 5P_{\frac{3}{2}} \rightarrow 5D_{\frac{3}{2},\frac{5}{2}}$ system, they have observed an absorption peak ([19]) along with expected transmission peaks. They demonstrate the absorption peak to be caused by TPA. They also developed an improved theoretical treatment for three-level ladder systems that accounts for all the absorption/transmission peaks from their systems, and highlight the fact that only if the transition is cyclic or almost cyclic the transmission peak that is observed can be due to EIT. Otherwise it arises from double-resonance optical pumping (DROP) [19]. Let us now analyse these three effects and their contribution in an actual three-level ladder type system as Moon et al. did, and try to match it to our experimental results.

Actual structure of a three-level ladder type system

The only true three-level ladder-type systems that can be found in atomic systems are the one with closed (or cyclic) transitions. One example is the $6S_{\frac{1}{2}}(F = 4) \rightarrow 6P_{\frac{3}{2}}(F' = 5) \rightarrow 5D_{\frac{5}{2}}(F'' = 6)$ transition in caesium, as the $5D_{\frac{5}{2}}$ state can only decay to the $6P_{\frac{3}{2}}$ state. Most three-level ladder systems have additional allowed decays channels from the upper state and to the other hyperfine ground state (dark ground state). These systems can be much better represented by a five-level ladder-type system (see Figure 4.13, [21]).

EIT, DROP and two-photon absorption

The contributions of the EIT, DROP and two-photon absorption in the five-levels ladder-type system for Moon et al. are explained below.

EIT　In a cycling transition (where $\gamma_{ij} = 0$ except for γ_{32} and γ_{43} in Figure 4.13), EIT tends to be the dominant phenomena with a weak probe (`Noh opt ex 2011`). However when the transition is not cycling, the additional decay rates tend to reduce the importance of the EIT for the amplitude of the transmission peak ([22]). The EIT tends to take a dispersive lineshape when the lasers are detuned.

DROP　DROP can be explained only in the five-levels ladder-type system. Here, a strong coupling tends to pump the atoms that are excited by the probe laser to the intermediate state in the dark ground state. Thus the population in the ground state decreases and the transmission is bigger. DROP increases with both probe and pump intensities. The lineshape of DROP does not show dispersive behaviour when the laser are detuned ([21], [19]).
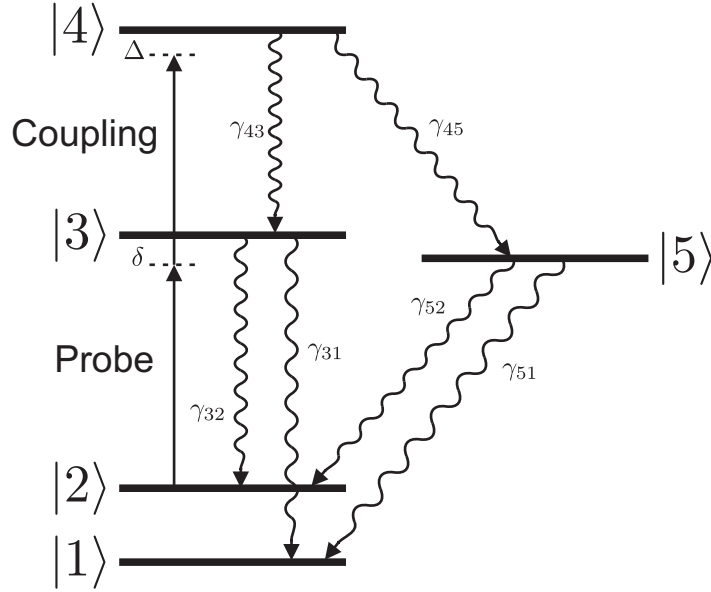
Figure 4.13: Scheme of a five-level ladder-type system.

Two-photon absorption   TPA appears when the two beams respect the two-photon resonance. It results in an absorption peak. TPA is always present, but mostly overcome by the one-photon effects EIT and DROP. Moon et al. explain the absorption peak that they observe by the fact that for this particular transition, EIT and DROP are too weak or suppressed. They observed that their absorption peak amplitude increases with the pump intensity but decreases with an increase of the probe intensity.

4.4.2   Comparison to our results

In our system, the upper state is a long-living state. Therefore the decay rates from this state are low. This would mean that DROP is more difficult to achieve as in Moon's system. Our intermediate state has additional decay paths to the direct $7P_{3/2} \rightsquigarrow 6S_{1/2}$. This leads to additional decoherence, which would tend to reduce the EIT contribution. The $F' = 5$ intermediate state however can decay in the dark ground state ($F = 3$) only via the additional decay paths mentioned in section 3.1. The $6S_{\frac{1}{2}}(F = 4) \rightarrow 7P_{\frac{3}{2}}(F' = 5) \rightarrow 32S$ transition is therefore not far from being cyclic, considering the long lifetime of the Rydberg state.

We observed that the absorption peak amplitude grows with the pump intensity. This is consistent with TPA. Moreover, we just mentioned that EIT and DROP effects should be inhibited compared to Moon's system. This can explain why we need relatively high intensities for the transmission processes (EIT and DROP) to take over the TPA and to observe a transition from absorption peaks to transmission peaks. The almost cyclic character of the $6S_{\frac{1}{2}}(F = 4) \rightarrow 7P_{\frac{3}{2}}(F' = 5) \rightarrow 32S$ transition is also consistent with the fact that in this case, we sometimes observe signals with a dispersive lineshape. In this case, the implied detuning could come from the blue laser, whose locking system was unstable at the time. All of this is consistent with the transition from absorption to transmission peaks as we increase the pump intensity for a constant probe intensity.

Therefore the work of Moon et al. helps us understand that because of the long-living character of the Rydberg state and the additional decay paths from the $7P_{3/2}$ state, the EIT and DROP effects are inhibited and they surpass the two-photon absorption process for higher intensities. The TPA is actually a weak effect, so this also explains why the measured signals were always

very weak and needed averaging to be distinguished.

Yet one conclusion of our experiment remains unexplained: the transition to enhanced absorption for higher pump intensities at constant probe intensities. Indeed increasing the pump intensity should increase the EIT and the optical pumping. Our results should be further investigated with simulations of the five-level ladder-type system. These simulations should focus on the influence of the existence of several decay paths from the $7P_{3/2}$ state, as it is the only change to the model compared to usual three-level ladder system $5S_{\frac{1}{2}} \to 5P_{\frac{3}{2}} \to nS, nD$ in rubidium, which exhibits strong EIT ([23]).

4.4.3 Other effects

Though the former interpretation appears to be robust, there are quite a few differences between our system and Moon's system (long-living upper state, inverted ratio of the wavenumbers, ...). Therefore we examined other hypotheses for the observation of enhanced absorption.

Fundamental aspects

Rydberg state In order to check if the $32S$ Rydberg state had a specificity (e.g. shorter lifetime) that would lead to the results that were observed, other Rydberg states were tried with both allowed azimuthal quantum numbers $L = 0$ and 2. The $35S$, $43S$, $32D$ states show identical behaviour to the $32S$ state.

Inverted wavenumber ratio One of the characteristic of our $6S_{\frac{1}{2}} \to 7P_{\frac{3}{2}} \to nS, nD$ approach is that the wavenumber ratio of the driven transitions is inverted compared to usual systems. The laser with the largest wavenumber (shortest wavelength) drives the first transition (455 nm - 1070 nm) of our system whereas in the two well studied approaches via the D2-line in caesium and rubidium it is the smallest wavenumber first (780 nm - 480 nm in Rb, 852 nm - 509 nm in Cs). The consequence of this inversion on a ladder system is that the averaging over the Doppler velocity distribution is changed. However, simulations show that enhanced transmission should still be present at all Rabi frequencies/intensities. Also measurements on other "inverted" ladder systems have already been performed ([20], [18]) and enhanced transmission was reported. Ergo, the scheme having an inverted wavenumber ratio should not be the cause for the observation of enhanced absorption.

Broadening effects

Laser ionization Another hypothesis is that the infrared laser induced the ionization of the Rydberg atoms, explaining the peculiar effect that was measured. The level scheme is shown in Figure 4.14. Let us assume that the Rydberg atoms are ionized by the infrared laser driving the upper transition. Since we observe enhanced absorption for several Rydberg levels for which the resonant wavelengths differ by up to several nanometres, this phenomenon is not strongly dependant on the wavelength of this laser.

The ionization was tested with an additional laser passing through the cell. This is a diode-pumped Nd:YAG laser with 1.5 W of optical output power at 1064 nm. A scheme of the modified set-up is shown in Figure 4.15. The transmission of the blue laser was measured with and without additional laser. Like in the very-first measurements, the beams were focused in the cell to $100\,\mu$m. The probe beam was weak (power of $24\,\mu$W, intensity of approx. $10^3\,\mathrm{W/m^2}$). The results are shown in Figures 4.16(a) and 4.16(b). In both cases, strong and weak pump, the only visible difference between the two signals is a shift in frequency, which comes from the drift of the lasers. Therefore there is no laser ionization visible.
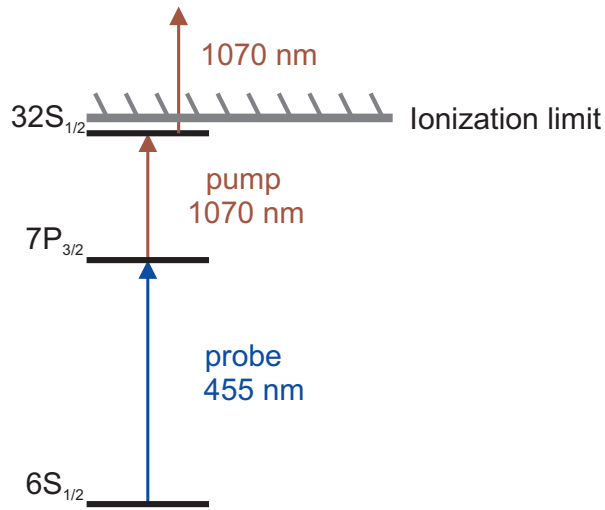
Figure 4.14: Level scheme corresponding to the ionization hypothesis.

Figure 4.15: Modified set-up with the additional beam propagating through the cell.

(a) Strong pump beam. Averaging: 8 takes

(b) Weak pump beam. Averaging: 256 takes

Figure 4.16: Blue laser transmission signal with the infrared laser being scanned. The pump beam was (a) strong (power of 95 mW (maximum available), intensity of approx. 10^8 W/m^2) and (b) weak (power of $440\,\mu$W, intensity of approx. 10^5 W/m^2).

Background gases and collisions A defect spectroscopy cell would possess an excessively high fraction of background gase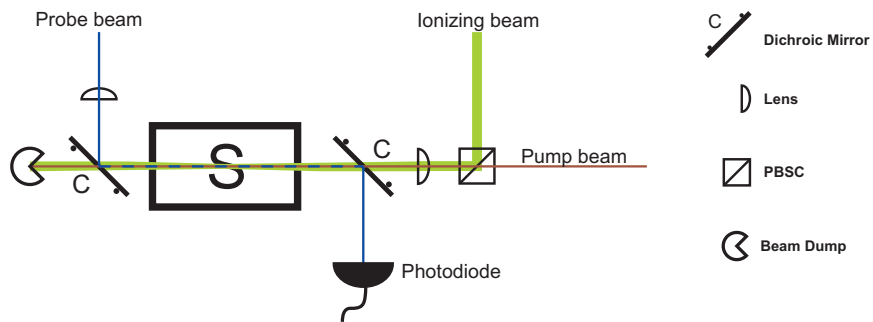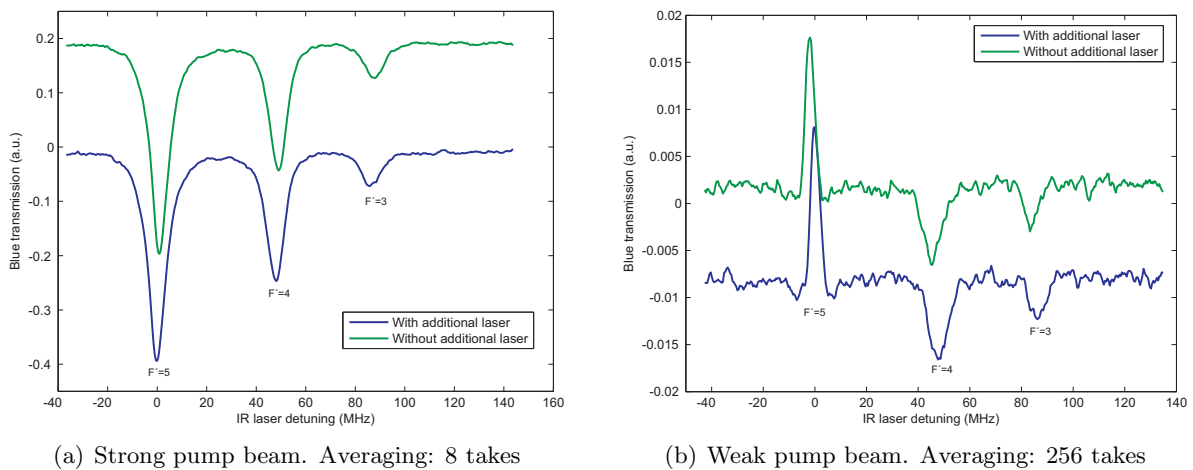s. These could be responsible for unwanted effects. This hypothesis was ruled out by trying a commercial Cs spectroscopy cell with which we noticed no difference compared to the home-made cell.

It has also been reported in [24] that collisions can induce enhanced absorption in ladder systems. A three level ladder system with collisional decay rates was simulated and the results exhibit a competition between EIT and enhanced absorption as a function of the probe Rabi frequency. We also witnessed such a phenomena except that Yang sees the absorption taking over the transmission as he increases the probe Rabi frequency and we measured the exact opposite. Moreover the atomic density that is achieved in our spectroscopy cell at around $60\,°C$ on the order of $10^{18}\,\text{atoms/m}^3$. This value is way below the collisional regime. The combination of these arguments allows us to say that our measurement results are not a result of collisions.

Chapter 5

Conclusion and outlook

The scope of this thesis has been the set-up of a new laser system and to investigate a two-photon transition to a Rydberg state in caesium via an intermediate state. First results on the behaviour of the transition have been presented and explained by applying a five-level atom model.

The first transition $6S_{\frac{1}{2}} \rightarrow 7P_{\frac{3}{2}}$ was driven by a commercial frequency doubled diode laser. The laser could be frequency locked to the hyperfine transitions with the DAVLL spectroscopy method and saturation absorption spectroscopy. A measurement method to determine temperature of the spectroscopy cell was reported and led to satisfying results.

The excitation to a Rydberg state was performed with a commercial diode laser. Surprisingly, the measurements did not match the expected results. Enhanced absorption of the blue laser was observed at the two-photon resonance instead of the expected EIT signal. To gain more insight the intensity dependence of the system was studied and the transition between absorption and transmission peaks was determined. A more complex model than the usual three-level system as well as the comparison with other results on three-level systems allowed to determine that the results arose from the competition between three processes, and in particular that the enhanced absorption was due to two-photon absorption. A set of simulations has to be performed on five-levels systems, in order to make sure that the interpretation was right, and to further understand the role of the different parameters in the system.

As mentioned above, the original purpose of the set-up was to perform EIT measurement and to lock the second laser frequency with this signal. The conclusion of this study is that such a procedure would be highly consuming in optical power, as obtaining clean spectra at low pump power required substantial averaging. The recently developed method of polarisation spectroscopy of an excited state transition ([25]) will be performed to lock the frequency of the 1070 nm laser. We have good confidence that this method will produce better signals, as it relies on the optical pumping on the first transition by a circularly polarised beam. Although the optical pumping should not be as efficient as in a closed transition, the almost cyclic nature of the $6S_{\frac{1}{2}}(F = 4) \rightarrow 7P_{\frac{3}{2}}(F' = 5)$ transition should still make it possible to create an anisotropy for the 1070 nm laser.

Once the laser set-up is fully functional, the goal is to amplify the 1070 nm laser in a fibre amplifier, to modulate its intensity with an ultrafast Pockels cell and to study fast dynamics on the $6S_{\frac{1}{2}} \rightarrow 7P_{\frac{3}{2}} \rightarrow nS, nD$ transition, similarly to previous work on rubidium ([3]). Afterwards, we would like to achieve higher caesium densities and to observe blockade phenomena in a vapour cell.

Appendix A

Caesium level structure
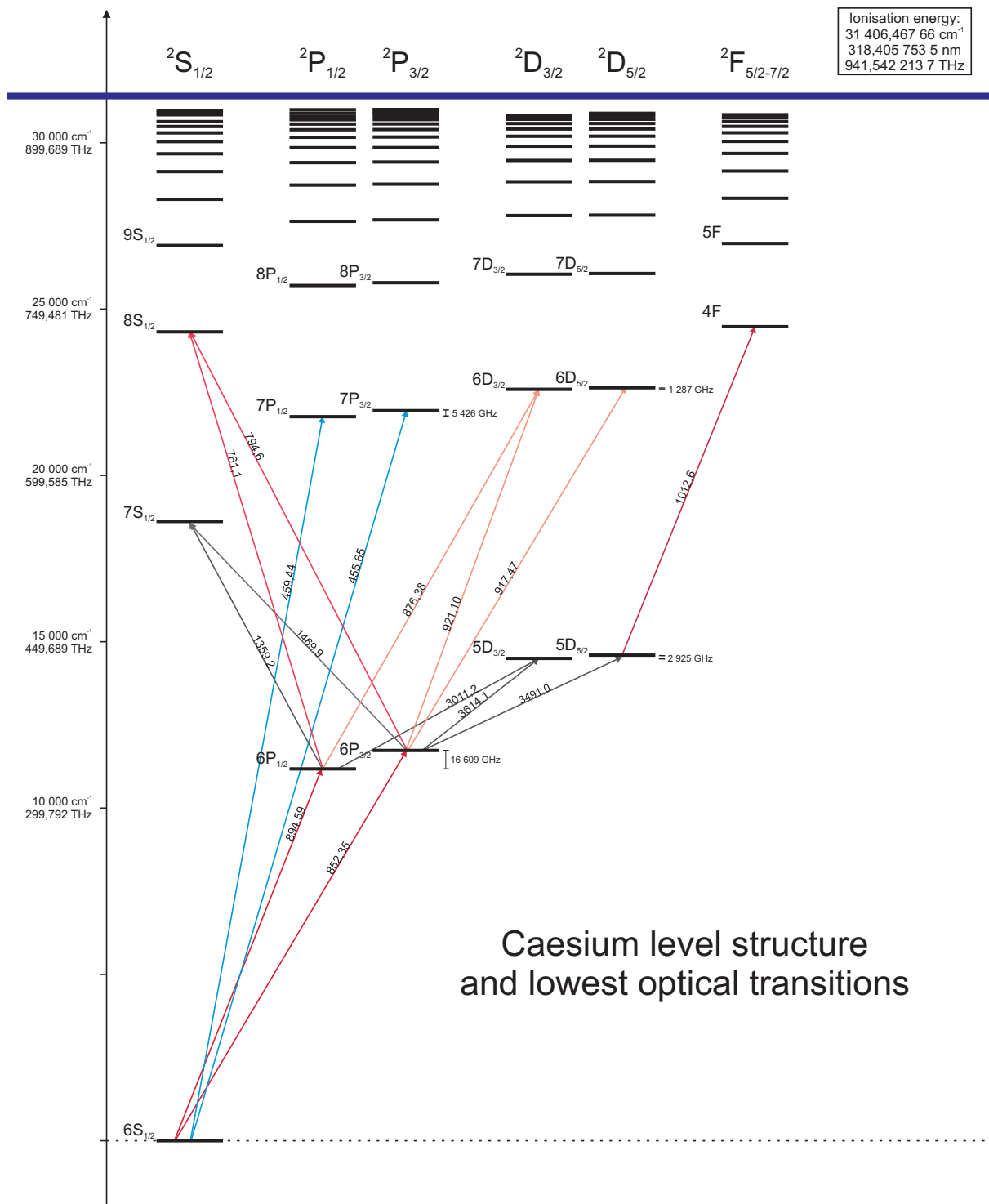
Figure A.1: Level structure and lowest optical transitions of caesium. The wavelength of each transition is indicated on the arrow representing the transition. The values were taken or calculated from [26], [27] and [28] with the best available precision.
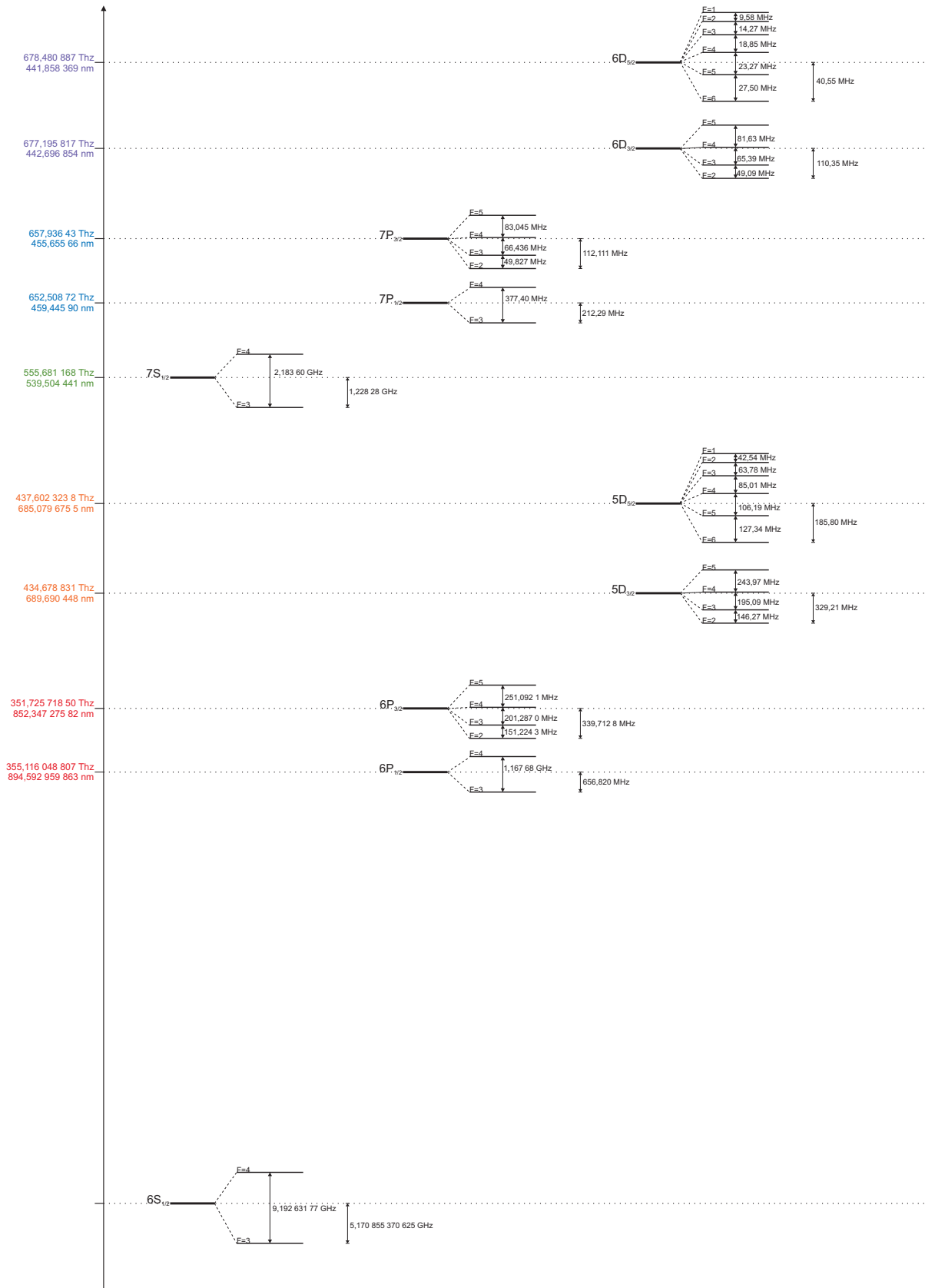
Figure A.2: Hyperfine structure of the lowest energy levels of caesium. The values were taken or calculated from [4] and [29].

Appendix B

Dipole matrix elements: derivation and analysis

B.1   Derivation of the dipole matrix elements

B.1.1   The spherical basis

A very useful tool for the evaluation of the dipole matrix elements is the so-called **spherical basis**, since it provides a very nice and convenient form for the dipole operator using the spherical harmonics. The overview presented here is based on the treatment of the spherical basis by Steck [30], Sobelman [31] or Zare [32].

In terms of the Cartesian basis vectors $\hat{x}$, $\hat{y}$ and $\hat{z}$, the spherical basis vectors are defined as:

$$\hat{e}_{\pm 1} := \mp \frac{1}{\sqrt{2}}(\hat{x} \pm i\hat{y}) = -(\hat{e}_{\mp 1})^*$$
$$\hat{e}_0 := \hat{z} = (\hat{e}_0)^*$$

(B.1)

Note that we must use a hermitian scalar product so that this basis is orthonormal: $\hat{e}_{+1} \cdot \hat{e}_{+1} = 0$ but $(\hat{e}_{+1})^* \cdot \hat{e}_{+1} = 1$.

The components of any vector $\boldsymbol{A}$ in the spherical basis are given by : $A_q := \hat{e}_q \cdot \boldsymbol{A}$ (usual "dot" product!), and thus the expression of $\boldsymbol{A}$ in the spherical basis is:

$$\boldsymbol{A} = \sum_q A_q \hat{e}_q^* = \sum_q (-1)^q A_q \hat{e}_{-q}$$

(B.2)

The hermitian scalar product is then defined as $\boldsymbol{A}^* \cdot \boldsymbol{B} = \sum_q (A_q)^* B_q$ so that the norm is $|\boldsymbol{A}|^2 = \sum_q |A_q|^2$.

If the components of a vector $\boldsymbol{A}$ are defined in the Cartesian and spherical basis such that $\boldsymbol{A} = A_x \hat{x} + A_y \hat{y} + A_z \hat{z} = \sum_q A_q \hat{e}_q^*$, the the basis transformation relations are:

$$A_0 = A_z \qquad\qquad A_z = A_0$$
$$A_{\pm 1} = \mp \frac{1}{\sqrt{2}}(A_x \pm iA_y) \qquad\qquad A_x = -\frac{1}{\sqrt{2}}(A_{+1} - A_{-1})$$
$$A_y = \frac{i}{\sqrt{2}}(A_{+1} + A_{-1})$$

(B.3)

We can now express the components of the position operator $\boldsymbol{r}$ in the spherical basis:

$$r_{\pm 1} = \mp \frac{r}{\sqrt{2}} \sin\theta e^{\pm i\varphi}$$
$$r_0 = r\cos\theta$$

(B.4)

or more compactly,

$$r_q = r\sqrt{\frac{4\pi}{3}}Y_{1q}(\theta, \varphi) \tag{B.5}$$

As we can see later on (equation (B.7)), the q term corresponds to the inverse of the polarisation: $q = 0$ is π-polarisation, $q = +1$ is σ^--polarisation and $q = -1$ is σ^+-polarisation.

$$r_q = r \underset{47}{} Y_{1q}(\theta, \varphi) \tag{B.5}$$

B.1.2 Reduced matrix element, what is it?

A dipole matrix element $\langle jm_j|er_q|j'm_j'\rangle$ can be factored as a product of a radial and an angular dependance using the Wigner-Eckart theorem:

$$\langle jm_j|er_q|j'm_j'\rangle = \langle j\|e\boldsymbol{r}\|j'\rangle\langle jm_j|j'm_j',1\,q\rangle \tag{B.6}$$

$$\langle jm_j|er_q|j'm_j'\rangle = \langle j\|e\boldsymbol{r}\|j'\rangle(-1)^{j-m_j}\sqrt{2j+1}\begin{pmatrix} j & 1 & j' \\ -m_j & q & m_j' \end{pmatrix} \tag{B.7}$$

$$\langle jm_j|er_q|j'm_j'\rangle = \langle j\|e\boldsymbol{r}\|j'\rangle(-1)^{j'-1+m_j}\sqrt{2j+1}\begin{pmatrix} j' & 1 & j \\ m_j' & q & -m_j \end{pmatrix} \tag{B.8}$$

respectively with Clebsch-Gordan coefficients or Wigner 3-j symbols.

Without hyperfine structure or LS-coupling, such a dipole matrix element can also be written in an integral form and expanded using the separation of the radial and angular part of the wave function (symmetries of the Hamiltonian operator).

$$
\begin{aligned}
\langle Lm_L|er_q|L'm_L'\rangle &= \langle Lm_L|er\sqrt{\tfrac{4\pi}{3}}Y_{1\,q}|L'm_L'\rangle && \text{using equation (B.5)} \tag{B.9}\\[4pt]
&= e\sqrt{\frac{4\pi}{3}}\int_{r,\theta,\varphi}(R_{n\,L}^*\,r\,R_{n'\,L'}r^2\,dr)(Y_{L\,m_L}^*Y_{1\,q}Y_{L'\,m_L'}\sin\theta\,d\theta\,d\varphi) \tag{B.10}\\[4pt]
&= e\sqrt{\frac{4\pi}{3}}\left(\int_r r^3 R_{n\,L}^* R_{n'\,L'}\,dr\right)(-1)^{m_L}\sqrt{\frac{(2L+1)(2\times1+1)(2L'+1)}{4\pi}}\\
&\quad\times\begin{pmatrix} L & 1 & L' \\ 0 & 0 & 0 \end{pmatrix}\begin{pmatrix} L & 1 & L' \\ -m_L & q & m_{L'} \end{pmatrix}_1 \tag{B.11}\\[4pt]
&= e(-1)^{m_L}\left(\int_r r^3 R_{n\,L}^* R_{n'\,L'}\,dr\right)\sqrt{(2L+1)(2L'+1)}\\
&\quad\times\begin{pmatrix} L & 1 & L' \\ 0 & 0 & 0 \end{pmatrix}\begin{pmatrix} L & 1 & L' \\ -m_L & q & m_{L'} \end{pmatrix} \tag{B.12}
\end{aligned}
$$

We can now identify the equation (B.7), valid for any angular momentum, with the equation (B.12) to get the expression of the the reduced dipole matrix element $\langle L\|e\boldsymbol{r}\|L'\rangle$.

$$\langle L\|e\boldsymbol{r}\|L'\rangle = e(-1)^{m_L-(L-m_L)}\left(\int_r r^3 R_{n\,L}^* R_{n'\,L'}\,dr\right)\sqrt{2L'+1}\begin{pmatrix} L & 1 & L' \\ 0 & 0 & 0 \end{pmatrix} \tag{B.13}$$

Since

$$\begin{pmatrix} L & 1 & L' \\ 0 & 0 & 0 \end{pmatrix} = \begin{cases} \sqrt{\dfrac{L_{max}}{(2L+1)(2L'+1)}}(-1)^{\frac{L+L'+1}{2}} & \text{if } \Delta L = \pm 1 \\ 0 & \text{if } \Delta L \neq \pm 1 \end{cases} \tag{B.14}$$

with $L_{max} = \max(L,L')$, we get

$$\langle L\|e\boldsymbol{r}\|L'\rangle = e(-1)^{2m_L-L}\left(\int_r r^3 R_{n\,L}^* R_{n'\,L'}\,dr\right)\sqrt{2L'+1}\sqrt{\frac{L_{max}}{(2L+1)(2L'+1)}}(-1)^{\frac{L+L'+1}{2}} \tag{B.15}$$

$$= e(-1)^{\frac{L'-L+1}{2}}\left(\int_r r^3 R_{n\,L}^* R_{n'\,L'}\,dr\right)\sqrt{\frac{L_{max}}{2L+1}} \qquad m_L\in\mathbb{N}\text{ so }(-1)^{2m_L}=1 \tag{B.16}$$

if $\Delta L = \pm 1$, and $\langle L\|e\boldsymbol{r}\|L'\rangle = 0$ otherwise.

---

[1]Here we use $Y_{l\,-m} = (-1)^m Y_{l\,m}$ and equation (B.67), taken from [32] eq. (3.119) p. 103, or citesobelman eq. (4.62) p.66

We can also define a "purely radial" dipole matrix element as:

$$\langle R_{n\,L}|er|R_{n'\,L'}\rangle = e\int_r r^3 R^*_{n\,L} R_{n'\,L'}\,dr \tag{B.17}$$

The relation between this *radial* dipole matrix element and the *reduced* dipole matrix element $\langle L\|e\boldsymbol{r}\|L'\rangle$ coming from the Wigner-Eckhart theorem is then:

$$\langle L\|e\boldsymbol{r}\|L'\rangle = (-1)^{\frac{L'-L+1}{2}}\sqrt{\frac{L_{max}}{2L+1}}\langle R_{n\,L}|er|R_{n'\,L'}\rangle \tag{B.18}$$

The *radial* dipole matrix element $\langle R_{n\,L}|er|R_{n'\,L'}\rangle$ is simply the radial integration of the radial parts of the wave functions. It is used for example in [1]. The *reduced* dipole matrix element $\langle L\|e\boldsymbol{r}\|L'\rangle$ used for example by Steck, coming from the Wigner-Eckhart theorem, contains an additional *angular* factor, depending on the L's.

B.1.3 Calculation of the dipole matrix element with hyperfine structure

A hyperfine sublevel can be split in a sum of uncoupled products of fine structure and nucleus spin sublevels using the Clebsch-Gordan coefficients or the Wigner 3-j symbols:

$$|nLSJIFm_F\rangle = \sum_{\substack{m_J,m_I \\ m_J+m_I=m_F}} |Jm_J, Im_I\rangle\langle Jm_J, Im_I|Fm_F\rangle \tag{B.19}$$

$$|Fm_F\rangle = \sum_{\substack{m_J,m_I \\ m_J+m_I=m_F}} |Jm_J\rangle|Im_I\rangle\sqrt{2F+1}(-1)^{J-I+m_F} \begin{pmatrix} J & I & F \\ m_J & m_I & -m_F \end{pmatrix} \tag{B.20}$$

Similarly,

$$|nLSJm_J\rangle = \sum_{\substack{m_L,m_S \\ m_L+m_S=m_J}} |Lm_L, Sm_S\rangle\langle Lm_L, Sm_S|Jm_J\rangle \tag{B.21}$$

$$|Jm_J\rangle = \sum_{\substack{m_L,m_S \\ m_L+m_S=m_J}} |Lm_L\rangle|Sm_S\rangle\sqrt{2J+1}(-1)^{L-S+m_J} \begin{pmatrix} L & S & J \\ m_L & m_S & -m_J \end{pmatrix} \tag{B.22}$$

Putting this expression in the $|Fm_F\rangle$ expression, we obtain:

$$|Fm_F\rangle = \sqrt{(2F+1)(2J+1)}(-1)^{J-I+L-S}$$
$$\times \sum_{\substack{m_J+m_I=m_F \\ m_L+m_S=m_J}} |Lm_L\rangle|Sm_S\rangle|Im_I\rangle(-1)^{m_F+m_J} \begin{pmatrix} L & S & J \\ m_L & m_S & -m_J \end{pmatrix} \begin{pmatrix} J & I & F \\ m_J & m_I & -m_F \end{pmatrix} \tag{B.23}$$

Let us now write the complete formula for the dipole matrix element with hyperfine structure $\langle Fm_F|er_q|F'm'_F\rangle$ using equations (B.23) and (B.7), and reduce it to get equation (B.8) in terms of F. The relations used to manipulate the Wigner 3-j symbols and Wigner 6-j symbols are listed in section B.3.

$$\langle Fm_F|er_q|F'm'_F\rangle = \sqrt{(2F+1)(2J+1)}\sqrt{(2F'+1)(2J'+1)}(-1)^{J-I+L-S}(-1)^{J'-I'+L'-S'}$$

$$\times \sum_{\substack{m_J+m_I=m_F\\ m_L+m_S=m_J\\ m'_J+m'_I=m'_F\\ m'_L+m'_S=m'_J}} \langle Im_I|\langle Sm_S|\langle Lm_L|er_q|L'm'_L\rangle|S'm'_S\rangle|I'm'_I\rangle(-1)^{m_F+m_J}(-1)^{m'_F+m'_J}$$

$$\times \begin{pmatrix} L & S & J \\ m_L & m_S & -m_J \end{pmatrix}\begin{pmatrix} J & I & F \\ m_J & m_I & -m_F \end{pmatrix}\begin{pmatrix} L' & S' & J' \\ m'_L & m'_S & -m'_J \end{pmatrix}\begin{pmatrix} J' & I' & F' \\ m'_J & m'_I & -m'_F \end{pmatrix} \quad (B.24)$$

$$= \sqrt{(2F+1)(2J+1)}\sqrt{(2F'+1)(2J'+1)}(-1)^{J+J'+L+L'-I-I'-S-S'}$$

$$\times \sum \delta_{II'}\delta_{m_Im'_I}\delta_{SS'}\delta_{m_Sm'_S}\langle Lm_L|er_q|L'm'_L\rangle(-1)^{m'_F+m_F+m'_J+m_J}$$

$$\times \begin{pmatrix} L & S & J \\ m_L & m_S & -m_J \end{pmatrix}\begin{pmatrix} L' & S' & J' \\ m'_L & m'_S & -m'_J \end{pmatrix}\begin{pmatrix} J & I & F \\ m_J & m_I & -m_F \end{pmatrix}\begin{pmatrix} J' & I' & F' \\ m'_J & m'_I & -m'_F \end{pmatrix} \quad (B.25)$$

$$= {}^1\sqrt{(2F+1)(2J+1)}\sqrt{(2F'+1)(2J'+1)}(-1)^{J+J'+L+L'-2I-2S}$$

$$\times \sum_{\substack{m_J+m_I=m_F\\ m_L+m_S=m_J\\ m'_J+m_I=m'_F\\ m'_L+m_S=m'_J}} (-1)^{m'_F+m_F+m'_J+m_J}(-1)^{L-m_L}\sqrt{2L+1}\langle L\|er\|L'\rangle\begin{pmatrix} L & 1 & L' \\ -m_L & q & m'_L \end{pmatrix}$$

$$\times \begin{pmatrix} L & S & J \\ m_L & m_S & -m_J \end{pmatrix}\begin{pmatrix} L' & S & J' \\ m'_L & m_S & -m'_J \end{pmatrix}\begin{pmatrix} J & I & F \\ m_J & m_I & -m_F \end{pmatrix}\begin{pmatrix} J' & I & F' \\ m'_J & m_I & -m'_F \end{pmatrix} \quad (B.26)$$

---

[1]Since the dipole operator doesn't act on the electronic and nucleic spin, the Kronecker-δ symbols in equation (B.25) come from the fact that electronic spin and nucleic spin states form an orthonormal basis. This is the reason why there is only I, m_I, S and m_S left in equation (B.26). We also use equation (B.7) for $\langle Lm_L|er_q|L'm'_L\rangle$

$$\langle Fm_F|er_q|F'm_F'\rangle =^2 \sqrt{(2F+1)(2J+1)}\sqrt{(2F'+1)(2J'+1)}\sqrt{2L+1}(-1)^{J+J'+L-2I-3S}$$

$$\times \sum_{\substack{m_J+m_I=m_F \\ m_L+m_S=m_J \\ m_J'+m_I=m_F' \\ m_L'+m_S=m_J'}} (-1)^{m_F'+m_F-m_J+4m_S}\langle L\|er\|L'\rangle \begin{pmatrix} J & I & F \\ m_J & m_I & -m_F \end{pmatrix}\begin{pmatrix} J' & I & F' \\ m_J' & m_I & -m_F' \end{pmatrix}$$

$$\times (-1)^{L+L'+S+m_L+m_L'-m_S} \underbrace{\begin{pmatrix} J' & S & L' \\ m_J' & -m_S & -m_L' \end{pmatrix}}\begin{pmatrix} L & 1 & L' \\ -m_L & q & m_L' \end{pmatrix}\begin{pmatrix} L & S & J \\ m_L & m_S & -m_J \end{pmatrix} \qquad \text{(B.27)}$$

$$=^3 \sqrt{(2F+1)}\sqrt{(2F'+1)(2J+1)}(-1)^{J+J'+L-2I+S}$$

$$\times \sum_{\substack{m_J+m_I=m_F \\ m_J'+m_I=m_F'}} (-1)^{m_F'+m_F-m_J}\begin{pmatrix} J & I & F \\ m_J & m_I & -m_F \end{pmatrix}\begin{pmatrix} J' & I & F' \\ m_J' & m_I & -m_F' \end{pmatrix}\begin{pmatrix} J' & 1 & J \\ m_J' & q & -m_J \end{pmatrix}(-1)^{-J'-L-1-S}$$

$$\times \underbrace{(-1)^{J'+L+1+S}\langle L\|er\|L'\rangle\sqrt{(2J'+1)(2L+1)}\begin{Bmatrix} J' & 1 & J \\ L & S & L' \end{Bmatrix}}_{=\langle J\|er\|J'\rangle} \qquad \text{(B.28)}$$

$$=^4 \sqrt{(2F+1)}\sqrt{(2F'+1)(2J+1)}(-1)^{J+J'+L-2I+S}$$

$$\times \sum \langle J\|er\|J'\rangle(-1)^{m_F'+m_F-m_J}\begin{pmatrix} J & I & F \\ m_J & m_I & -m_F \end{pmatrix}\begin{pmatrix} J' & I & F' \\ m_J' & m_I & -m_F' \end{pmatrix}\begin{pmatrix} J' & 1 & J \\ m_J' & q & -m_J \end{pmatrix}(-1)^{-J'-L-1-S} \qquad \text{(B.29)}$$

---

[2]The relation $m_J'+m_J-m_L=(m_L'+m_L-m_S)+(-m_J+4m_S)$ has been used to transform the exponent of (-1). The underbracketed 3-j symbol was also transformed using the symmetry relations (B.57) and (B.58).

[3]We use the fact that $(-1)^{4S}=1=(-1)^{4m_S}$ to suppress the $4m_S$ exponent and transform $(-1)^{-3S}$ into $(-1)^S$. We also factorised 3 3-j symbols into one 3-j symbol and one 6-j symbol using the tranformation formula (B.66).

[4]We used the equation (37) from [4] to introduce the fine structure $\langle J\|er\|J'\rangle$ reduced dipole matrix element. Symmetry relations (B.63) and (B.64) are used to get the proper form for the 6-j symbol.

$$\langle Fm_F|er_q|F'm'_F\rangle = {}^5\sqrt{(2F+1)}\sqrt{(2F'+1)(2J+1)}(-1)^{J-2I-1}$$

$$\times \sum \langle J\|e\boldsymbol{r}\|J'\rangle(-1)^{m'_F+m_F-m_J}\underbrace{(-1)^{J+I+F}\begin{pmatrix} F & I & J \\ -m_F & m_I & m_J \end{pmatrix}}\begin{pmatrix} J' & 1 & J \\ m'_J & q & -m_J \end{pmatrix}\underbrace{(-1)^{J'+I+F'}\begin{pmatrix} J' & I & F' \\ -m'_J & -m_I & m'_F \end{pmatrix}} \quad \text{(B.30)}$$

$$= {}^6\sqrt{(2F+1)}\sqrt{(2F'+1)(2J+1)}(-1)^{J-I-1+F'+F}$$

$$\times \sum_{\substack{m_J+m_I=m_F \\ m'_J+m_I=m'_F}} \langle J\|e\boldsymbol{r}\|J'\rangle(-1)^{2m'_F+m_F-2m_I}$$

$$\times (-1)^{J'+J+I+m_I-m'_J-m_J}\begin{pmatrix} F & I & J \\ -m_F & m_I & m_J \end{pmatrix}\begin{pmatrix} J' & 1 & J \\ m'_J & q & -m_J \end{pmatrix}\begin{pmatrix} J' & I & F' \\ -m'_J & -m_I & m'_F \end{pmatrix} \quad \text{(B.31)}$$

$$= {}^7\sqrt{(2F+1)}\sqrt{(2F'+1)(2J+1)}(-1)^{J-I-1+F'+F+2m'_F+m_F-2I}$$

$$\times \sum_{\substack{m_J+m_I=m_F \\ m'_J+m_I=m'_F}} \langle J\|e\boldsymbol{r}\|J'\rangle(-1)^{J'+J+I+m_I-m'_J-m_J}\begin{pmatrix} F & I & J \\ -m_F & m_I & m_J \end{pmatrix}\begin{pmatrix} J' & 1 & J \\ m'_J & q & -m_J \end{pmatrix}\begin{pmatrix} J' & I & F' \\ -m'_J & -m_I & m'_F \end{pmatrix} \quad \text{(B.32)}$$

$$= {}^8\sqrt{(2F+1)}(-1)^{J-3I-1+F'+F+2m'_F+m_F}\begin{pmatrix} F & 1 & F' \\ -m_F & q & m'_F \end{pmatrix}(-1)^{-F'-J-1-I}$$

$$\times \underbrace{(-1)^{F'+J+1+I}\langle J\|e\boldsymbol{r}\|J'\rangle\sqrt{(2F'+1)(2J+1)}\begin{Bmatrix} F & 1 & F' \\ J' & I & J \end{Bmatrix}}_{=\langle F\|e\boldsymbol{r}\|F'\rangle}$$

$$\quad \text{(B.33)}$$

---

[5] The two underbracketed 3-j symbols were transformed using respectively (B.57) and (B.58).

[6] The exponent of (-1) was modified using the relation $m'_F + m_F - m_J = (2m'_F + m_F - 2m_I) + (m_I - m'_J - m_J)$.

[7] Since $-2I$ and $-2m_I$ have the same parity, we use $(-1)^{-2I} = (-1)^{-2m_I}$.

[8] We factorised 3 3-j symbols into one 3-j symbol and one 6-j symbol using the tranformation formula (B.66).

$$\langle Fm_F|er_q|F'm'_F\rangle = {}^9\sqrt{(2F+1)}(-1)^{-4I+F-2+2m'_F+m_F}\langle F\|e\boldsymbol{r}\|F'\rangle(-1)^{F'+1+F}\begin{pmatrix}F' & 1 & F\\ m'_F & q & -m_F\end{pmatrix} \tag{B.34}$$

$$= (-1)^{2F-4I+2m'_F}\langle F\|e\boldsymbol{r}\|F'\rangle(-1)^{F'-1+m_F}\sqrt{(2F+1)}\begin{pmatrix}F' & 1 & F\\ m'_F & q & -m_F\end{pmatrix} \tag{B.35}$$

$$\langle Fm_F|er_q|F'm'_F\rangle = {}^{10}\langle F\|e\boldsymbol{r}\|F'\rangle(-1)^{F'-1+m_F}\sqrt{(2F+1)}\begin{pmatrix}F' & 1 & F\\ m'_F & q & -m_F\end{pmatrix} \tag{B.36}$$

$$\tag{B.37}$$

---

[9]We used the equation (36) from [4] to introduce the fine structure $\langle F\|e\boldsymbol{r}\|F'\rangle$ reduced dipole matrix element. Symmetry relations (B.63), (B.64) and (B.57) are used to get the proper form for the 6-j symbol, as well as another 3-j symbol.

[10]Finally, to get equation (B.36), which is exactly the same as the equation (35) from [4], we used the following facts:

- $2F$ and $2F'$ necessarily have the same parity, so $2F$ and $2m'_F$ too, so $(-1)^{2F+2m'_F} = 1$
- I is an integer or a half integer, so $(-1)^{-4I} = 1$

B.1.4 Comments

Why Wigner 6-j symbols?

We saw in the calculation that Wigner 6-j symbols appear by recombination of Wigner 3-j symbols. We can understand this in another way. Let us remember that the Wigner 6-j symbols come from the different possibilities of adding three angular momenta. Adding j_1, j_2, j_3 gives different basis if you first add $j_1 + j_2 = j_{12}$ and then $j_{12} + j_3$, or if you first add $j_2 + j_3 = j_{23}$ and then $j_1 + j_{23}$. The Wigner 6-j symbols give the basis transformation relations.

$$\langle F \| e\boldsymbol{r} \| F' \rangle = \langle J \| e\boldsymbol{r} \| J' \rangle (-1)^{F'+J+1+I} \sqrt{(2F'+1)(2J+1)} \begin{Bmatrix} J & J' & 1 \\ F' & F & I \end{Bmatrix}$$

In this equation (equation (36) from [4], similar to equation (37)), the idea is that one can see the photon as either changing J or F. This amounts to coupling the photon (of angular momentum 1) to the electron (of angular momentum J) either before or after coupling the electron to the nucleus (of angular momentum I). Thus the appearance of the Wigner 6-j symbol.

The equation (37) from [4] is to understand in the similar way, that is coupling the photon to the electron (of angular momentum L) before or after coupling the electron to the electronic spin S.

For more details, you can refer to Daniel Steck's very comprehensive script on quantum optics [30], sections 7.3.6.1 and 7.3.7.1.

Angular factor / Transition strength

Let's now write the dipole matrix element for the transition from a state $|nL \cdots \alpha\, m_\alpha\rangle$ to a state $|n'L' \cdots \alpha'\, m'_\alpha\rangle$, the α angular momenta being either L, J or F, in terms of the reduced or the radial dipole matrix elements multiplied by an angular factor $\{\cdot|\cdot\}$ (often also refered to as transition strength):

$$\langle nL \cdots \alpha\, m_\alpha | e r_q | n'L' \cdots \alpha'\, m'_\alpha \rangle = \langle L \| e\boldsymbol{r} \| L' \rangle \times \{L \cdots \alpha\, m_\alpha | L' \cdots \alpha'\, m'_\alpha\}_{reduced} \tag{B.38}$$

$$\langle nL \cdots \alpha\, m_\alpha | e r_q | n'L' \cdots \alpha'\, m'_\alpha \rangle = \langle R_{n\,L} | er | R_{n'\,L'} \rangle \times \{L \cdots \alpha\, m_\alpha | L' \cdots \alpha'\, m'_\alpha\}_{radial} \tag{B.39}$$

The relation between these two angular factors is then:

$$\{L \cdots \alpha\, m_\alpha | L' \cdots \alpha'\, m'_\alpha\}_{reduced} = (-1)^{\frac{L'-L+1}{2}} \sqrt{\frac{2L+1}{L_{max}}} \{L \cdots \alpha\, m_\alpha | L' \cdots \alpha'\, m'_\alpha\}_{radial} \tag{B.40}$$

These angular factors exhibit different symmetry properties:

$$\{L' \cdots \alpha'\, m'_\alpha | L \cdots \alpha\, m_\alpha\}_{reduced} = (-1)^{\varepsilon} \sqrt{\frac{2L+1}{2L'+1}} \{L \cdots \alpha\, m_\alpha | L' \cdots \alpha'\, m'_\alpha\}_{reduced} \tag{B.41}$$

$$\{L' \cdots \alpha'\, m'_\alpha | L \cdots \alpha\, m_\alpha\}_{radial} = (-1)^{\kappa} \{L \cdots \alpha\, m_\alpha | L' \cdots \alpha'\, m'_\alpha\}_{radial} \tag{B.42}$$

where ε and κ are two integers.

Using the reduced dipole matrix elements, we can also define transition strengths between two angular momenta α and β, α and β being either L, J or F:

$$\langle n \cdots \alpha \cdots \beta\, m_\beta | e r_q | n' \cdots \alpha' \cdots \beta'\, m'_\beta \rangle = \langle \alpha \| e\boldsymbol{r} \| \alpha' \rangle \{\alpha \cdots \beta\, m_\beta | \alpha' \cdots \beta'\, m'_\beta\}_{reduced} \tag{B.43}$$

The symmetry relation in that case is:

$$\{\alpha' \cdots \beta'\, m'_\beta | \alpha \cdots \beta\, m_\beta\}_{reduced} = (-1)^{\eta} \sqrt{\frac{2\alpha+1}{2\alpha'+1}} \{\alpha \cdots \beta\, m_\beta | \alpha' \cdots \beta'\, m'_\beta\}_{reduced} \tag{B.44}$$

where η is an integer.

B.2 Discussions and examples

B.2.1 Normalizations

The dipole matrix elements obey several normalization, arising from the orthogonalization rules for the Clebsch-Gordan, Wigner 3-j and Wigner 6-j symbols. They also have physical interpretations.

Let us first consider the decay from a state $|j'm'\rangle$ to any other state $|j\,(m'+q)\rangle$. The corresponding decay rate is then[1]:

$$\Gamma_{j'm'\to j\,(m'+q)} = \frac{\omega_0^3}{3\pi\epsilon_0\hbar c^3}|\langle j\,(m'+q)|er_q|j'm'\rangle|^2 \tag{B.45}$$

The global decay rate from the state $|j'm'\rangle$ is the sum of all possible single decay rates:

$$\Gamma_{j'm'} = \sum_{j,q}\Gamma_{j'm'\to j\,(m'+q)} \tag{B.46}$$

$$\Gamma_{j'm'} = \frac{\omega_0^3}{3\pi\epsilon_0\hbar c^3}\sum_{j,q}|\langle j\,(m'+q)|er_q|j'm'\rangle|^2 \tag{B.47}$$

The sum of all possible transition strengths to a single state $|j'm'\rangle$ is appearing. The Wigner-Eckhart theorem (B.7 and B.6) and the first orthogonality relation for the Wigner 3-j coefficients (B.60) yield:

$$\sum_{j,q}|\langle j\,(m'+q)|er_q|j'm'\rangle|^2 = \sum_{j,q}|\langle j\|e\boldsymbol{r}\|j'\rangle|^2|\langle j\,(m'+q)|1\,q,j'm'\rangle|^2 \tag{B.48}$$

$$\sum_{j,q}|\langle j\,(m'+q)|er_q|j'm'\rangle|^2 = \sum_{j,q}|\langle j\|e\boldsymbol{r}\|j'\rangle|^2\,(2j+1)\begin{pmatrix} j & 1 & j' \\ -(m'+q) & q & m' \end{pmatrix}^2 \tag{B.49}$$

$$\sum_{j,q}|\langle j\,(m'+q)|er_q|j'm'\rangle|^2 = \sum_{j}|\langle j\|e\boldsymbol{r}\|j'\rangle|^2\,\frac{2j+1}{2j'+1} \tag{B.50}$$

Assuming a simple $j\to j'$ system, the sum disappears and we get:

$$\sum_{j,q}|\langle j\,(m'+q)|er_q|j'm'\rangle|^2 = |\langle j\|e\boldsymbol{r}\|j'\rangle|^2\,\frac{2j+1}{2j'+1} \tag{B.51}$$

This identity can be verified by summing the squared coefficients leading to a single level in Figure B.1. A similar relation is valid if we express the reduced dipole matrix element in another basis (equation (36) from [4], leading to the equation (38)) and use the orthogonality relation for the Wigner 6-j coefficients:

$$\sum_{F,q}|\langle F\,(m'_F+q)|er_q|F'm'_F\rangle|^2 = \frac{2J+1}{2J'+1}|\langle J\|e\boldsymbol{r}\|J'\rangle|^2 \quad \text{(equation (40) in [4])} \tag{B.52}$$

This normalization is actually valid for any angular momenta and can be rewritten in terms of (reduced) transition strengths (see equation (B.38)):

$$\sum_{\beta,m_\beta}|\{\alpha\cdots\beta\,m_\beta|\alpha'\cdots\beta'\,m'_\beta\}_{reduced}|^2 = \frac{2\alpha+1}{2\alpha'+1} \tag{B.53}$$

---

[1][30] section 7.3.7.4 or 11.4

The meaningful interpretation of this takes place when $j = j'$. In this case the strengths of the transitions leading to a single magnetic level is 1, meaning that adding the strengths of the different decay paths represent the probabilities of the single decays.
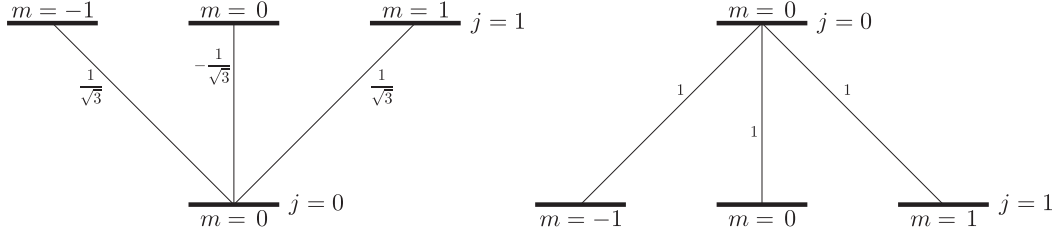

Figure B.1: Two-level-systems with the associated 'transition factors' (Clebsch-Gordan coefficients from equation (B.6) in this case).

Another normalization appears from the sum of all dipole matrix elements from a single ground state sublevel. This is also a consequence of the first orthogonality relation.
In [4], this normalization is shown with the equations (39), (41) and (42). The interpretation of this normalization is a bit tricky and not really physical (see [30]).

B.2.2   Hydrogen atom

The structure, fine structure and hyperfine structure of the $1s \rightarrow 2p$ transition of hydrogen (D1 and D2 line), with the respective transition coefficients, is represented in Figure B.2, Figure B.3, Figure B.4 and Figure B.5. The missing coefficients can be obtained by symmetry or antisymmetry: multiplication by $(-1)^{j'+j+1-2m_j}$, j and j' being the corresponding angular momenta. This factor arises from the symmetry relation (B.58) for the Wigner 3-j coefficients and from $m_j \rightarrow -m_j$.
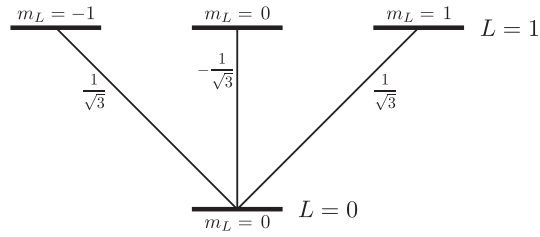
Figure B.2: 'L-structure' of the $1s \to 2p$ transition of hydrogen. The coefficients give the dipole matrix elements when multiplied with the reduced matrix element $\langle L\|e\boldsymbol{r}\|L'\rangle = \langle 0\|e\boldsymbol{r}\|1\rangle$
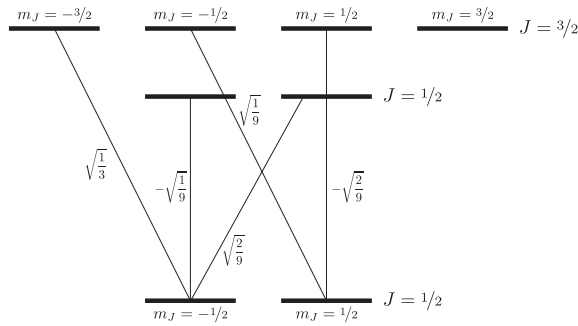

Figure B.3: 'J-structure' of the $1s \to 2p$ transition of hydrogen. The coefficients give the dipole matrix elements when multiplied with the reduced matrix element $\langle L\|e\boldsymbol{r}\|L'\rangle = \langle 0\|e\boldsymbol{r}\|1\rangle$

Figure B.4: 'F-structure' of the D1-line of hydrogen ($1s \to 2p$). The coefficients give the dipole matrix elements when multiplied with the reduced matrix element $\langle J\|e\boldsymbol{r}\|J'\rangle = \langle 1/2\|e\boldsymbol{r}\|1/2\rangle$. For the D1-line, $\langle J\|e\boldsymbol{r}\|J'\rangle = \sqrt{13/6}\langle L\|e\boldsymbol{r}\|L'\rangle$
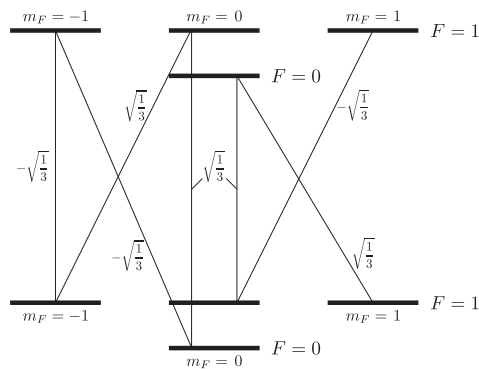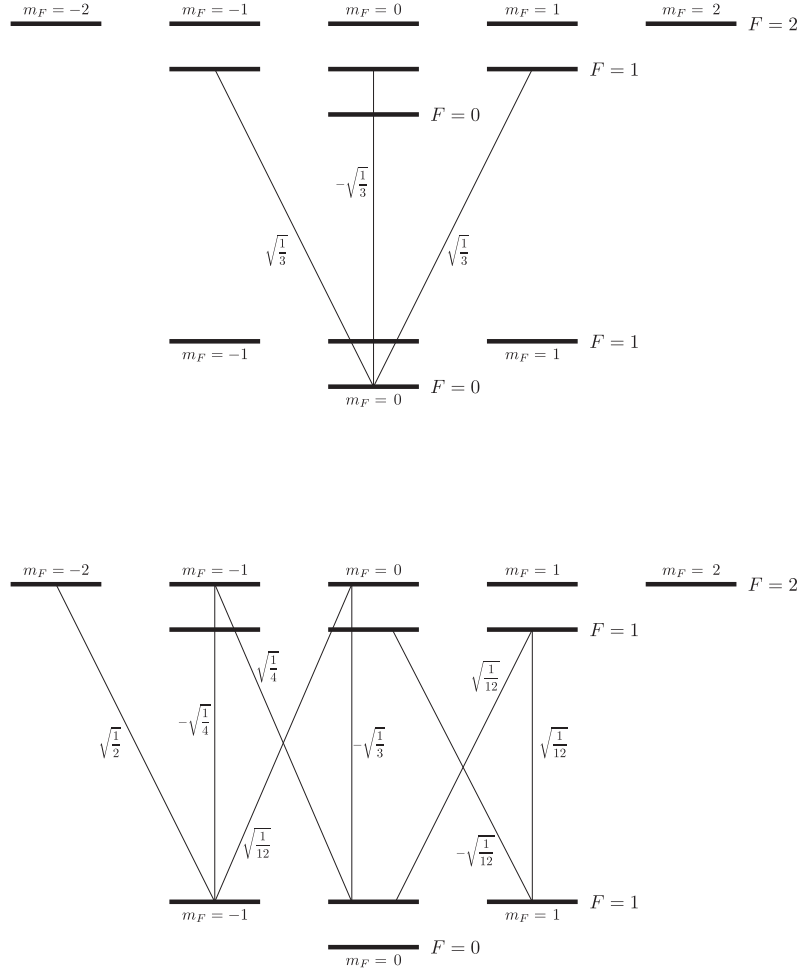
Figure B.5: 'F-structure' of the D2-line of hydrogen ($1s \rightarrow 2p$). The coefficients give the dipole matrix elements when multiplied with the reduced matrix element $\langle J \| e\boldsymbol{r} \| J' \rangle = \langle 1/2 \| e\boldsymbol{r} \| 3/2 \rangle$. For the D2-line, $\langle J \| e\boldsymbol{r} \| J' \rangle = -\sqrt{25/6}\langle L \| e\boldsymbol{r} \| L' \rangle$

B.3   Mathematical formulae

B.3.1   Wigner 3-j symbols and Clebsch-Gordan coefficients

The relation between Clebsch-Gordan Coefficients and Wigner 3-j symbols is:

$$\langle j_1 m_1, j_2 m_2 | j_3 m_3 \rangle = (-1)^{j_1 - j_2 + m_3} \sqrt{2j_3 + 1} \begin{pmatrix} j_1 & j_2 & j_3 \\ m_1 & m_2 & -m_3 \end{pmatrix} \tag{B.54}$$

Symmetry relations

- The "complex conjugate" of a Clebsch-Gordan coefficient is defined as:

$$\langle JM | j_1 m_1, j_2 m_2 \rangle \equiv \langle j_1 m_1, j_2 m_2 | JM \rangle \tag{B.55}$$

- The Wigner 3-j symbols have the following symmetry relations:

$$\begin{pmatrix} j_1 & j_2 & j_3 \\ m_1 & m_2 & m_3 \end{pmatrix} = \begin{pmatrix} j_2 & j_3 & j_1 \\ m_2 & m_3 & m_1 \end{pmatrix} = \begin{pmatrix} j_3 & j_1 & j_2 \\ m_3 & m_1 & m_2 \end{pmatrix} \tag{B.56}$$

$$\begin{aligned} \begin{pmatrix} j_1 & j_2 & j_3 \\ m_1 & m_2 & m_3 \end{pmatrix} &= (-1)^{j_1 + j_2 + j_3} \begin{pmatrix} j_1 & j_3 & j_2 \\ m_1 & m_3 & m_2 \end{pmatrix} \\ &= (-1)^{j_1 + j_2 + j_3} \begin{pmatrix} j_3 & j_2 & j_1 \\ m_3 & m_2 & m_1 \end{pmatrix} \\ &= (-1)^{j_1 + j_2 + j_3} \begin{pmatrix} j_2 & j_1 & j_3 \\ m_2 & m_1 & m_3 \end{pmatrix} \end{aligned} \tag{B.57}$$

$$\begin{pmatrix} j_1 & j_2 & j_3 \\ m_1 & m_2 & m_3 \end{pmatrix} = (-1)^{j_1 + j_2 + j_3} \begin{pmatrix} j_1 & j_2 & j_3 \\ -m_1 & -m_2 & -m_3 \end{pmatrix} \tag{B.58}$$

Orthogonality relations

The related orthogonality relations for Wigner 3-j symbols and Clebsch-Gordan coefficients are:

- First orthogonality relation:

$$\sum_{m_1, m_2} \langle jm | j_1 m_1, j_2 m_2 \rangle \langle j_1 m_1, j_2 m_2 | j' m' \rangle = \delta_{j,j'} \delta_{m,m'} \tag{B.59}$$

$$\sum_{m_1, m_2} \begin{pmatrix} j_1 & j_2 & j_3 \\ m_1 & m_2 & m_3 \end{pmatrix} \begin{pmatrix} j_1 & j_2 & j_3' \\ m_1 & m_2 & m_3' \end{pmatrix} = \frac{1}{2j_3 + 1} \delta_{j_3, j_3'} \delta_{m_3, m_3'} \tag{B.60}$$

- Second orthogonality relation:

$$\sum_{j,m} \langle j_1 m_1, j_2 m_2 | jm \rangle \langle jm | j_1 m_1', j_2 m_2' \rangle = \delta_{m_1, m_1'} \delta_{m_2, m_2'} \tag{B.61}$$

$$\sum_{j_3, m_3} (2j_3 + 1) \begin{pmatrix} j_1 & j_2 & j_3 \\ m_1 & m_2 & m_3 \end{pmatrix} \begin{pmatrix} j_1 & j_2 & j_3 \\ m_1' & m_2' & m_3 \end{pmatrix} = \delta_{m_1, m_1'} \delta_{m_2, m_2'} \tag{B.62}$$

Other relations can be found in Sobelman, or Zare for instance.

B.3.2 Wigner 6-j symbols

Symmetry relations

The Wigner 6-j symbols have the following symmetry relations:

$$\begin{Bmatrix} j_1 & j_2 & j_3 \\ l_1 & l_2 & l_3 \end{Bmatrix} = \begin{Bmatrix} j_2 & j_1 & j_3 \\ l_2 & l_1 & l_3 \end{Bmatrix} = \begin{Bmatrix} j_3 & j_2 & j_1 \\ l_3 & l_2 & l_1 \end{Bmatrix} = \begin{Bmatrix} j_1 & j_3 & j_2 \\ l_1 & l_3 & l_2 \end{Bmatrix} \tag{B.63}$$

$$\begin{Bmatrix} j_1 & j_2 & j_3 \\ l_1 & l_2 & l_3 \end{Bmatrix} = \begin{Bmatrix} l_1 & l_2 & j_3 \\ j_1 & j_2 & l_3 \end{Bmatrix} = \begin{Bmatrix} l_1 & j_2 & l_3 \\ j_1 & l_2 & j_3 \end{Bmatrix} = \begin{Bmatrix} j_1 & l_2 & l_3 \\ l_1 & j_2 & j_3 \end{Bmatrix} \tag{B.64}$$

Orthogonality relation

$$\sum_{j_3} (2j_6 + 1)(2j_3 + 1) \begin{Bmatrix} j_1 & j_2 & j_3 \\ j_4 & j_5 & j_6 \end{Bmatrix} \begin{Bmatrix} j_1 & j_2 & j_3 \\ j_4 & j_5 & j_6' \end{Bmatrix} = \delta_{j_6, j_6'} \tag{B.65}$$

Relation to the 3-j symbols   A sum of Wigner 3-j symbols can be factorised into a product of one 3-j symbol and one 6-j symbol using:

$$\sum_{\mu_1 \mu_2 \mu_3} (-1)^{l_1 + l_2 + l_3 + \mu_1 + \mu_2 + \mu_3} \begin{pmatrix} j_1 & l_2 & l_3 \\ m_1 & \mu_2 & -\mu_3 \end{pmatrix} \begin{pmatrix} l_1 & j_2 & l_3 \\ -\mu_1 & m_2 & \mu_3 \end{pmatrix} \begin{pmatrix} l_1 & l_2 & j_3 \\ \mu_1 & -\mu_2 & m_3 \end{pmatrix}$$

$$= \begin{pmatrix} j_1 & j_2 & j_3 \\ m_1 & m_2 & m_3 \end{pmatrix} \begin{Bmatrix} j_1 & j_2 & j_3 \\ l_1 & l_2 & l_3 \end{Bmatrix} \tag{B.66}$$

B.3.3   Other

$$\iint Y_{l_1 m_1} Y_{l_2 m_2} Y_{l_3 m_3} \sin \theta \, d\theta \, d\varphi$$

$$= \sqrt{\frac{(2\,l_1 + 1)(2\,l_2 + 1)(2\,l_3 + 1)}{4\pi}} \begin{pmatrix} l_1 & l_2 & l_3 \\ 0 & 0 & 0 \end{pmatrix} \begin{pmatrix} l_1 & l_2 & l_3 \\ m_1 & m_2 & m_3 \end{pmatrix} \tag{B.67}$$

Bibliography

[1] M. Saffman, T. G. Walker, and K. Mølmer, "Quantum information with Rydberg atoms," *Rev. Mod. Phys.*, vol. 82, pp. 2313–2363, Aug 2010. 6, 12, 49

[2] H. Kübler, J. P. Shaffer, T. Baluktsian, R. Löw, and T. Pfau, "Coherent excitation of Rydberg atoms in micrometre-sized atomic vapour cells," *Nature Photonics*, vol. 4, pp. 112–116, 2010. 6, 26

[3] B. Huber, T. Baluktsian, M. Schlagmüller, A. Kölle, H. Kübler, R. Löw, and T. Pfau, "Ghz rabi flopping to Rydberg states in hot atomic vapor cells," *Phys. Rev. Lett.*, vol. 107, p. 243001, Dec 2011. 6, 27, 42

[4] D. A. Steck, "Cesium D line data." available online at `http://steck.us/alkalidata` (revision 2.1.4, 23 December 2009). 7, 16, 45, 52, 54, 55, 56, 57

[5] H. Helm, "Dissipative processes in light-atom interactions." Lecture Notes, SS 2008. 7

[6] R. Daschner, "Frequenzmodulationsspektroskopie von Rydberg-Zuständen in Rubidium-Mikrozellen," diploma thesis, Universität Stuttgart, 5. Physikalisches Institut, 2011. 7

[7] T. Baluktsian, "Herstellung und Untersuchung mikrostrukturierter Rubidium-Spektroskopiezellen," diploma thesis, Universität Stuttgart, 4. Physikalisches Institut, 2008. 10

[8] K.-J. Boller, A. Imamoğlu, and S. E. Harris, "Observation of electromagnetically induced transparency," *Phys. Rev. Lett.*, vol. 66, pp. 2593–2596, May 1991. 12

[9] B. Gao, "Effects of Zeeman degeneracy on the steady-state properties of an atom interacting with a near-resonant laser field: Analytic results," *Phys. Rev. A*, vol. 48, pp. 2443–2448, Sep 1993. 13

[10] J. Sagle, R. K. Namiotka, and J. Huennekens, "Measurement and modelling of intensity dependent absorption and transit relaxation on the cesium D1-line," *Journal of Physics B: Atomic, Molecular and Optical Physics*, vol. 29, no. 12, p. 2629, 1996. 14

[11] A. A. Vasilyev, I. M. Savukov, M. S. Safronova, and H. G. Berry, "Measurement of the $6S - 7P$ transition probabilities in atomic cesium and a revised value for the weak charge Q_W," *Phys. Rev. A*, vol. 66, p. 020101, Aug 2002. 15

[12] R. W. Schmieder, A. Lurio, W. Happer, and A. Khadjavi, "Level-crossing measurement of lifetime and hfs constants of the $^2P_{\frac{3}{2}}$ states of the stable alkali atoms," *Phys. Rev. A*, vol. 2, pp. 1216–1228, Oct 1970. 15, 16

[13] O. S. Heavens, "Radiative transition probabilities of the lower excited states of the alkali metals," *J. Opt. Soc. Am.*, vol. 51, pp. 1058–1061, Oct 1961. 16

[14] T. Petelski, M. Fattori, G. Lamporesi, J. Stuhler, and G.M. Tino, "Doppler-free spectroscopy using magnetically induced dichroism of atomic vapor: a new scheme for laser frequency locking," *Eur. Phys. J. D*, vol. 22, no. 2, pp. 279–283, 2003. 17

[15] A. Grabowski, *Aufbau einer Messapparatur zur Laserkühlung und hochauflösende Rydberg-Spektroskopie an 87 Rb-Atomen.* PhD thesis, Universität Stuttgart, 2006. 26, 27

[16] Z.-G. Feng, L.-J. Zhang, J.-M. Zhao, C.-Y. Li, and S.-T. Jia, "Lifetime measurement of ultracold caesium Rydberg states," *Journal of Physics B: Atomic, Molecular and Optical Physics*, vol. 42, no. 14, p. 145303, 2009. 27

[17] T. Vogt, M. Viteau, J. Zhao, A. Chotia, D. Comparat, and P. Pillet, "Dipole blockade at förster resonances in high resolution laser excitation of Rydberg states of cesium atoms," *Phys. Rev. Lett.*, vol. 97, p. 083003, Aug 2006. 27

[18] N. Hayashi, A. Fujisawa, H. Kido, K.-I. Takahashi, and M. Mitsunaga, "Interference between electromagnetically induced transparency and two-step excitation in three-level ladder systems," *J. Opt. Soc. Am. B*, vol. 27, pp. 1645–1650, Aug 2010. 37, 39

[19] H. S. Moon and H. R. Noh, "Optical pumping effects in ladder-type electromagnetically induced transparency of $5S_{1/2}$–$5P_{3/2}$–$5D_{3/2}$ transition of ^{87}Rb atoms," *Journal of Physics B: Atomic, Molecular and Optical Physics*, vol. 44, no. 5, p. 055004, 2011. 37

[20] H. S. Moon, W. K. Lee, L. Lee, and J. B. Kim, "Double resonance optical pumping spectrum and its application for frequency stabilization of a laser diode," *Appl. Phys. Lett.*, vol. 85, no. 18, pp. 3965–3967, 2004. 37, 39

[21] H. S. Moon, L. Lee, and J. B. Kim, "Double resonance optical pumping effects inelectromagnetically induced transparency," *Opt. Express*, vol. 16, pp. 12163–12170, Aug 2008. 37

[22] H.-R. Noh and H. S. Moon, "Discrimination of one-photon and two-photon coherence parts in electromagnetically induced transparency for a ladder-type three-level atomic system," *Opt. Express*, vol. 19, pp. 11128–11137, Jun 2011. 37

[23] A. K. Mohapatra, T. R. Jackson, and C. S. Adams, "Coherent optical detection of highly excited Rydberg states using electromagnetically induced transparency," *Phys. Rev. Lett.*, vol. 98, p. 113003, Mar 2007. 39

[24] X. Yang, J. Sheng, and M. Xiao, "Electromagnetically induced absorption via incoherent collisions," *Phys. Rev. A*, vol. 84, p. 043837, Oct 2011. 41

[25] C. Carr, C. S. Adams, and K. J. Weatherill, "Polarization spectroscopy of an excited state transition," 2011. `arXiv:1107.2582v2 [physics.atom-ph]`. 42

[26] K.-H. Weber and C. J. Sansonetti, "Accurate energies of nS, nP, nD, nF, and nG levels of neutral cesium," *Phys. Rev. A*, vol. 35, pp. 4650–4660, Jun 1987. 44

[27] C. Moore, *Atomic Energy Levels, Vol. III (Molybdenum through Lanthanum and Hafnium through Actinium).* Circular of the National Bureau of Standards 467, U.S. Government Printing Office, Washington, DC, 1958. 44

[28] C. J. Lorenzen and K. Niemax, "Precise quantum defects of nS, nP and nD levels in Cs I," *Zeitschrift für Physik A Hadrons and Nuclei*, vol. 315, pp. 127–133, 1984. 44

[29] J. E. Sansonetti, "Wavelengths, transition probabilities, and energy levels for the spectra of cesium (Cs I - Cs LV)," *J. Phys. Chem. Ref. Data*, vol. 38, no. 4, pp. 761–923, 2009. 45

[30] D. A. Steck, "Quantum and atom optics." available online at `http://steck.us/teaching` (revision 0.8.2, 6 December 2011). 46, 55, 56, 57

[31] I. Sobelman, *Atomic spectra and radiative transitions*. Springer series in chemical physics, Springer-Verlag, 1979. 46

[32] R. Zare, *Angular momentum: understanding spatial aspects in chemistry and physics*. George Fisher Baker non-resident lectureship in chemistry at Cornell University, Wiley, 1988. 46, 48

Acknowledgements

I would like to express my gratitude to the people who were supporting me during this thesis and who made it possible for me to even consider doing it.

First of all I would like to thank Prof. Dr. Tilman Pfau for giving me the opportunity to start this very interesting project. I am sure a lot of other surprising things will happen again on this project!

I am thankful to Prof. Dr. Dressel for co-examining my thesis and for the interesting discussions.

I am very grateful to Dr. Robert Löw for giving me the will to come to atomic physics thanks to his lecture, and for being always available whenever I had a question.

I am extremely happy that I spent the last year working on the third floor. Special thanks go to Thomas "Balu" for the support in writing this thesis and for the dedicated proofreading, Harald for being always easily available, Andreas and Bernhard for the teaching in the beginning, Paul and Georg for the movies references, and Daniel, Lara, Michael, Renate and Ralf for participating to the great atmosphere of the MicCell team. I hope you didn't get annoyed when the language barrier came around.

I would also like to thank the people at l'École Centrale Paris, my "home" university in Paris, for giving me the great opportunity to come in Stuttgart. I am also thankful to Prof. Denninger for organizing the exchange at the University of Stuttgart.

And last but not least, un grand merci à ma famille pour leur soutien permanent, même si je n'arrive pas toujours à leur expliquer ce que je fais. Merci à mes parents pour m'avoir toujours poussé à la découverte, et à mon frère et ma soeur pour l'ambiance de fratrie bien sympa.